Supplementary Information (SI) for Energy & Environmental Science.

Supporting Information

“Head Surgery” of Polycyclic *o*-Quinones with Cyanated Aromatic Rings towards High Electron Mobility Acceptors Enable 19.6% Additive-Free Binary Organic Solar Cells

Tainan Duan, Jia Wang, Xiaochan Zuo, Yanyi Zhong, Yuhong Long, Peiran Wang, Kaihuai Tu, Cheng Zhong, Jiangbin Zhan, Oleg A. Rakitin, Zhaoyang Yao, Xiangjian Wan, Yan Zhao, Bin Kan, and Yongsheng Chen

Content:

1. Materials and Methods

All reactions were performed under nitrogen atmosphere and solvents were purified and dried from appropriate drying agents using standard techniques prior to use. Polymer donor **D18**, was purchased from HYPER. Ltd. Reagents available from commercial sources were used without further purification unless otherwise stated.

All unreported compounds were characterized by NMR spectroscopy on Bruker Avance III Ultrashield Plus instruments (400 and 600 MHz). High-resolution mass spectrometry (HR-MS) data of new acceptors were recorded using a Bruker solariX XR platform.

2. Synthetic Protocols and Characterizations

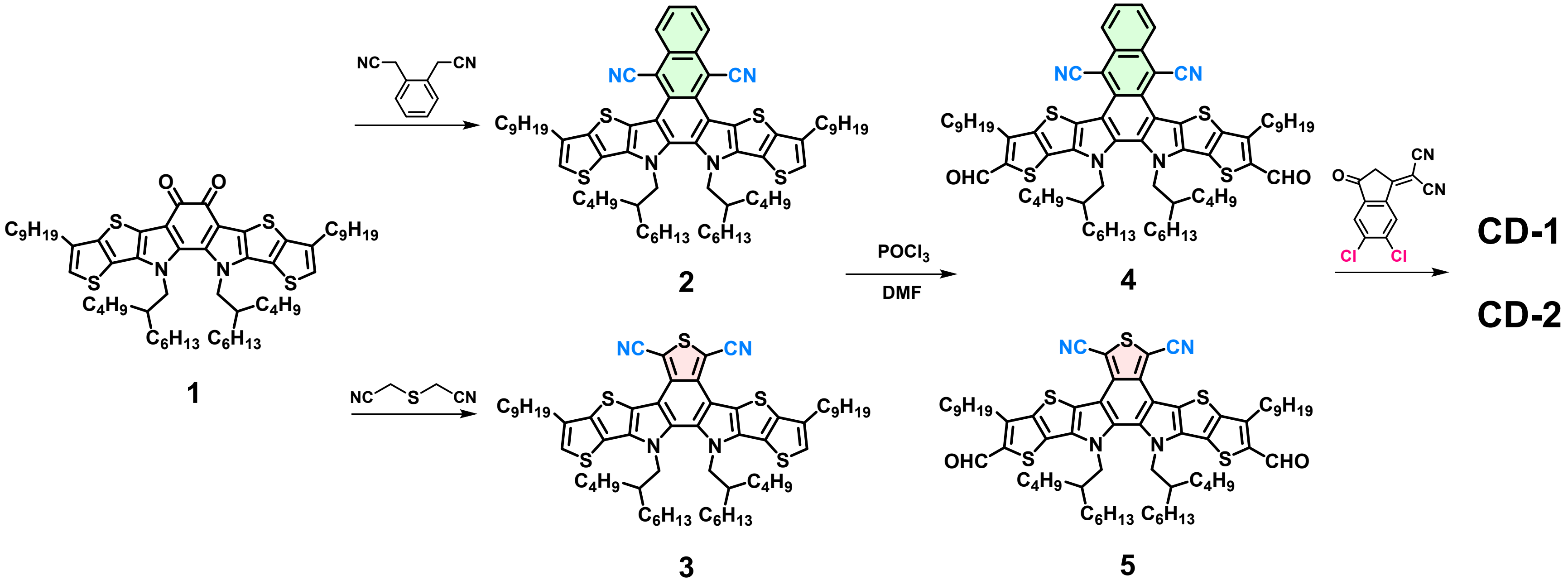

Scheme S1. Synthetic route of the new acceptors. *o*-Quinone **1** and thiodiacetonitrile were synthesized via reported procedures.[1,2]

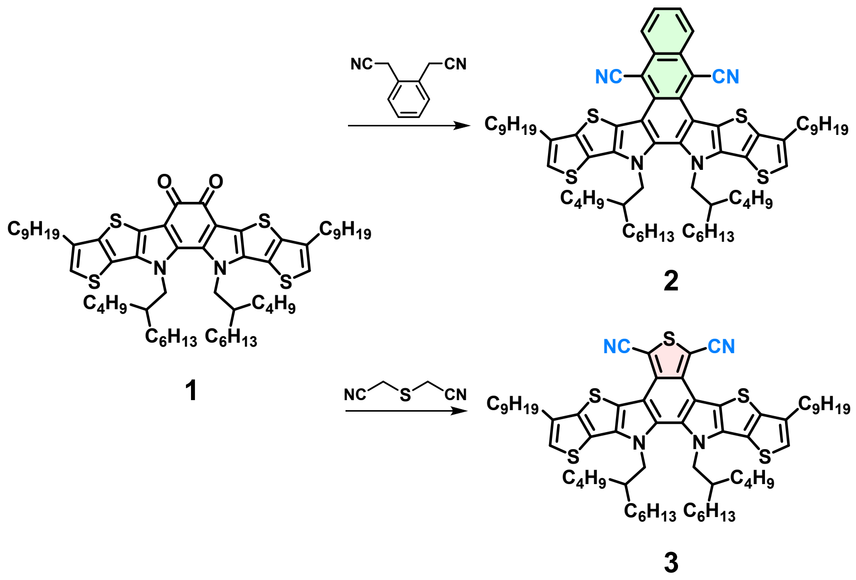

General procedure for the preparation of compound 2 and 3: In a round-bottom flask, compound **1** (1.0 equiv.) and dinitrile (o-xylylene dicyanide or thiodiacetonitrile, 2.0 equiv.) in piperidine (15 mL) was added water (2.5 mL). The reaction mixture was heated to 90 °C and stirred for 24 h. Next, the mixture was concentrated under reduced pressure. The crude product was purified by column chromatography over SiO_2 using hexanes/CH_2Cl_2 (3:1) as the eluent, affording target compound **2** or **3**.

Compound 2: Blue solid (230 mg, 85%). ^1H NMR (400 MHz, $CDCl_3$, δ ppm): 8.68-8.66 (m, 2H), 7.88-7.86 (m, 2H), 7.05 (s, 2H), 4.65 (d, *J* = 7.6 Hz, 4H), 2.89 (t, *J* = 7.6 Hz, 4H), 1.98 (br, 2H), 1.91-1.84 (m, 4H), 1.47-0.65 (m, 74H). ^{13}C NMR (101 MHz, $CDCl_3$, δ ppm): 143.87, 137.06, 136.78, 131.56, 130.06, 129.06, 128.60, 125.51, 124.41, 122.69, 119.96, 117.89, 115.14, 105.63, 54.54, 38.31, 32.01, 31.68, 29.69, 29.60, 29.57, 29.50, 29.45, 28.92, 22.93, 22.79, 22.57, 14.22, 14.05, 13.88.

Compound 3: Purple solid (195 mg, 87%). ^1H NMR (400 MHz, $CDCl_3$, δ ppm): 7.04 (s, 1H), 4.54 (d, *J* = 7.6 Hz, 4H), 2.83 (t, *J* = 7.6 Hz, 4H), 1.97-1.95 (m, 2H), 1.87-1.80 (m, 4H), 1.43-0.60 (m, 74H). ^{13}C NMR (101 MHz, $CDCl_3$, δ ppm): 143.39, 137.77, 137.74, 136.88, 135.88, 132.18, 123.17, 122.98, 122.94, 120.07, 114.72, 111.93, 101.19, 54.87, 38.71, 31.99, 31.67, 29.66, 29.53, 29.49, 29.42, 28.85, 27.00, 22.88, 22.82, 22.77, 22.60, 14.19, 14.07, 14.05, 13.82, 13.75.

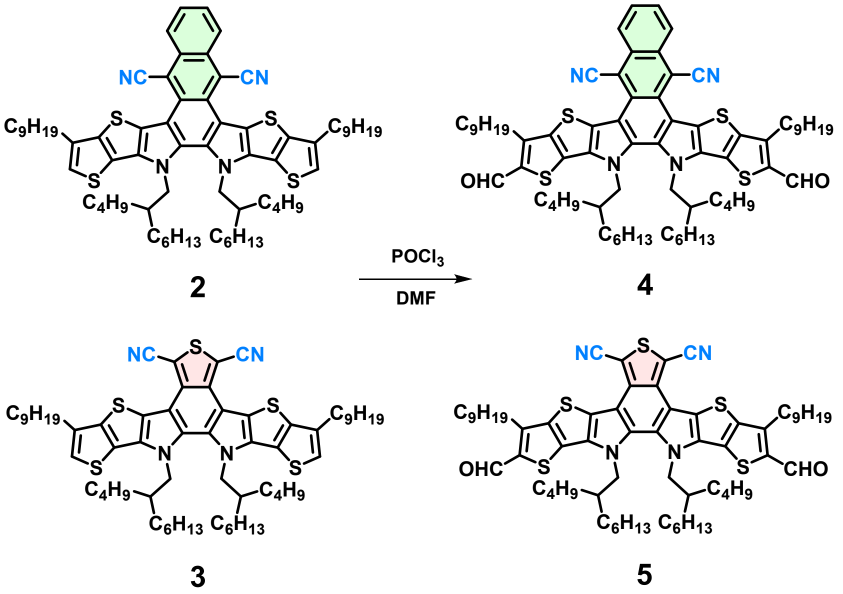

General procedure for the preparation of the dialdehyde 4 and 5: In a pre-dried round-bottom flask, compound **2** or **3** (1.0 equiv.), $POCl_3$ (20 equiv.) and DMF (40 equiv.) were dissolved in anhydrous 1,2-dichloroethane (20 mL). The reaction mixture was heated to 90 °C and was stirred for 24 h under argon atmosphere. Next, the mixture was cooled down and quenched with saturated sodium acetate solution (50 mL). The mixture was extracted with $CHCl_3$ (3×50 mL), and the organic phase was combined, dried over Na_2SO_4, filtered, and concentrated under reduced pressure. The crude product was purified by column chromatography over SiO_2 using hexanes/CH_2Cl_2 (1:1) as the eluent to yield the pure dialdehyde.

Compound 4: Crimson solid (161 mg, 70%). ^1H NMR (400 MHz, $CDCl_3$, δ ppm): 10.17 (s, 2H), 8.68-8.66 (m, 2H), 7.94-7.91 (m, 2H), 4.66 (d, J = 7.6 Hz, 4H), 3.26 (t, J = 7.6 Hz, 4H), 1.97-1.90 (m, 6H), 1.51-1.46 (m, 4H), 1.37-0.64 (m, 70H). ^{13}C NMR (101 MHz, $CDCl_3$, δ ppm): 181.90, 146.69, 144.43, 137.75, 136.62, 132.74, 130.34, 129.27, 129.04, 128.96, 128.44, 125.60, 117.52, 115.56, 106.22, 54.79, 38.57, 31.87, 31.58, 30.59, 29.72, 29.60, 29.49, 29.39, 29.30, 28.10, 26.92, 22.83, 22.68, 22.49, 14.12, 13.97, 13.78.

Compound 5: Reddish purple solid (153 mg, 68%). ^1H NMR (400 MHz, $CDCl_3$, δ ppm): 10.14 (s, 2H), 4.56 (d, J = 7.6 Hz, 4H), 3.21 (t, J = 7.6 Hz, 4H), 1.93-1.85 (m, 6H), 1.47-0.59 (m, 74H). ^{13}C NMR (101 MHz, $CDCl_3$, δ ppm): 181.87, 146.75, 144.07, 137.92, 137.40, 137.38, 135.63, 133.37, 128.91, 127.54, 127.51, 114.24, 112.49, 102.40, 55.11, 38.95, 31.86, 31.59, 30.58, 29.73, 29.52, 29.47, 29.41, 29.38, 29.29, 28.02, 22.80, 22.74, 22.68, 22.56, 22.54, 14.12, 14.02, 13.74, 13.69.

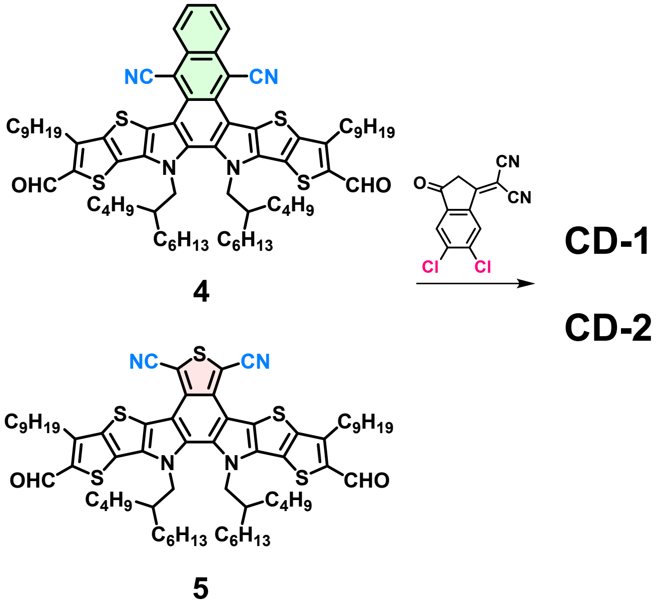

General procedure for the preparation of acceptors CD-1 and CD-2: To a mixed solution of the dialdehyde **4** or **5** (1.0 equiv.), (5,6-dichloro-3-oxo-2,3-dihydro-1H-inden-1-ylidene)malononitrile (2.5 equiv.) and acetate anhydride (20.0 equiv.) in toluene (20 mL), boron trifluoride etherate ($BF_3 \cdot OEt$, 5 equiv.) was added and the mixture was stirred for 20 min. Then the reaction mixture was quenched by adding methanol (50 mL), filtered, and washed with methanol (20 mL) and ethyl acetate (20 mL), affording the desired products in high yield and high purity. Further purification can be simply performed via re-precipitation method.

CD-1: Purple-black solid (110 mg, 93%). ^1H NMR (400 MHz, $CDCl_3$, δ ppm): 9.21 (s, 2H), 8.81 (s, 2H), 8.70-8.68 (m, 2H), 7.99-7.97 (m, 4H), 4.82 (br, 4H), 3.31 (t, *J* = 7.6 Hz, 4H), 2.04-2.01 (m, 2H), 1.92-1.88 (m, 4H), 1.54-0.67 (m, 74H). ^{13}C NMR (151 MHz, $CDCl_3$, δ ppm): 186.05, 158.71, 153.96, 145.96, 139.57, 139.22, 138.72, 137.08, 136.07, 135.89, 135.00, 133.94, 133.89, 132.73, 130.61, 129.77, 128.84, 126.91, 125.75, 124.96, 120.29, 117.28, 116.40, 114.97, 114.57, 106.87, 69.09, 55.08, 38.92, 31.87, 31.67, 31.42, 29.79, 29.74, 29.46, 29.30, 22.87, 22.67, 22.50, 14.12, 14.05, 13.80. FT-HR-MS: calcd. for $C_{96}H_{98}Cl_4N_8O_2S_4$ [m/z]: 1665.5454, found 1665.5522.

CD-2: Purple-blue solid (113 mg, 90%). ^1H NMR (400 MHz, $CDCl_3$, δ ppm): 9.17 (s, 2H), 8.79 (s, 2H), 7.95 (s, 2H), 4.72 (br, 4H), 3.23 (t, *J* = 7.6 Hz, 4H), 2.01-2.00 (m, 2H), 1.89-1.83 (m, 4H), 1.51-0.69 (m, 74H). ^{13}C NMR (151 MHz, $CDCl_3$, δ ppm): 186.03, 158.49, 153.87, 145.62, 139.57, 139.26, 138.66, 137.83, 136.00, 135.68, 135.50, 135.44, 134.67, 133.97, 131.15, 126.87, 124.95, 120.35, 114.91, 114.52, 113.95, 113.30, 103.35, 69.30, 55.60, 39.38, 31.86, 31.71, 31.68, 31.42, 29.70, 29.63, 29.47, 29.44, 29.30, 22.67, 22.60, 22.58, 14.15, 14.12, 13.83, 13.78. FT-HR-MS: calcd. for $C_{90}H_{94}Cl_4N_8O_2S_5$ [m/z]: 1620.4828, found 1621.4918.

3. Density Functional Theory (DFT) Calculations

For the isolated CD-1 and CD-2 molecules, the ground-state geometries were optimized at PBE0/def2-SVP level with Grimme's D3 dispersion correction with BJ dampening. All the alkyl chains were replaced with methyl groups. PCM solvation model was used for all the calculations with diphenylether (ε=3.73) as solvent to imitate the dielectric environment in solids. TD-DFT calculations were then performed on these geometries at ω-tuned LC-wHPBE level with omega set to 0.12. The ω was obtained using xwtune program. Corrected-linear response PCM solvation mode was used for CT and LE excited state. Multiwfn v3.8 was used to perform hole-electron analysis. All the DFT calculations were carried out using Gaussian 16 program.[3-7]

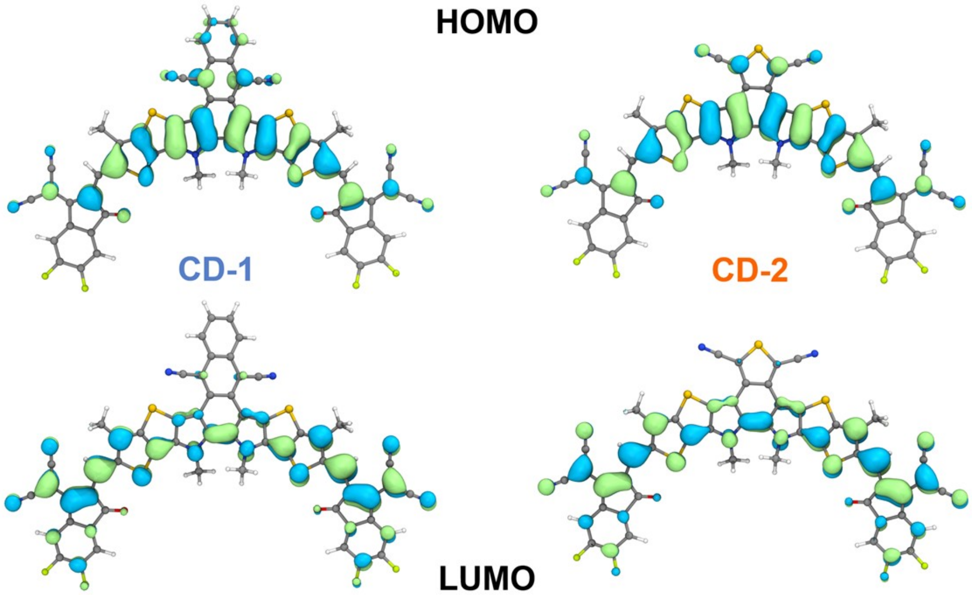

Figure S1. The frontier molecular orbits distribution of CD-1 and CD-2.

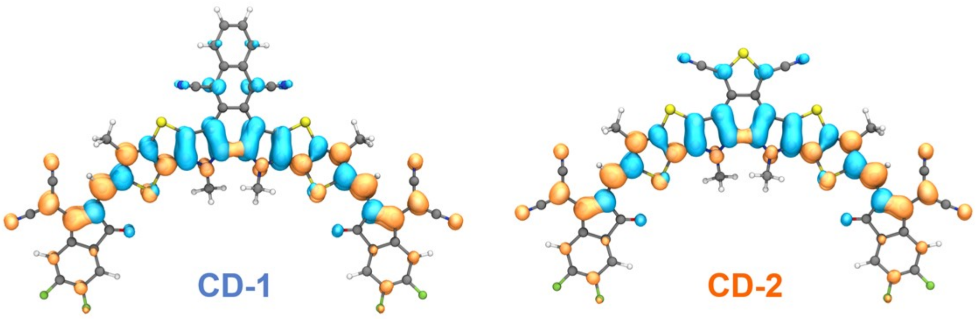

Figure S2. The hole(blue)-electron(yellow) distribution of acceptors calculated at relaxed S1 state.

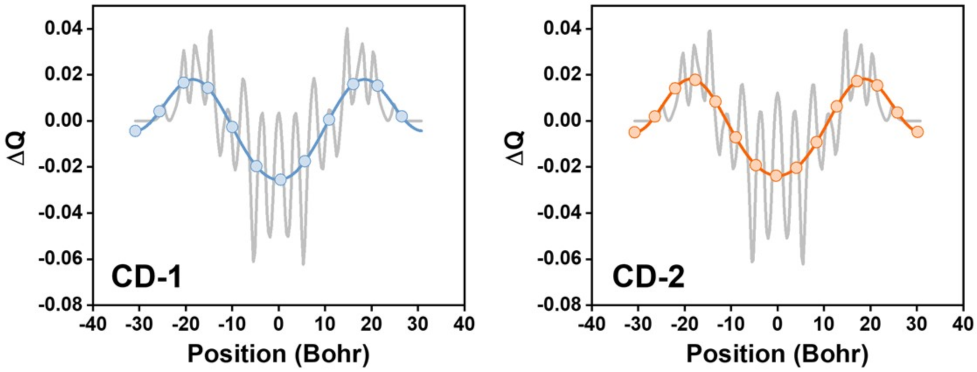

Figure S3. The theoretical density distribution ΔQ ($\Delta Q=\Psi^2_{LUMO}-\Psi^2_{HOMO}$) of CD-1 and CD-2.

Table S1. Excited state information of acceptors

Molecule	**sn**	**TE**[a] **(eV)**	**f**[b]	**D_idx**[c]	**Sr**[d]	**t_idx**[e]	**Orb. Comp.**[f]
CD-1	1	1.9565	1.8723	1.727	0.63721	-0.885	H-L:0.967
	2	2.2769	0.2572	2.166	0.59106	-0.463	H-L1:0.968
	3	2.2964	0.0406	3.281	0.55594	0.325	H-L2:0.956
CD-2	1	1.983	1.9816	1.64	0.64216	-0.829	H-L:0.977
	2	2.3113	0.2137	2.041	0.59475	-0.472	H-L1:0.963
	3	2.4256	0.0009	3.714	0.52106	1.117	H-L2:0.938;H-L3:0.033

[a] **TE**: the transition energy.

[b] **f**: the oscillator strength.

[c] **D_idx**: the centroid distance between hole and electron.

[d] **Sr**: the overlap integral of hole and electron.

[e] **t_idx**: the characteristic of excited state. The smaller the t_idx value, the stronger the LE feature, while the opposite indicates a stronger CT state.

[f] **Orb. Comp.**: the orbital composition of the S1 state.

4. Cyclic Voltammogram

Electrochemical measurements were performed with a LK98B II Microcomputer-based Electrochemical Analyzer, using a glassy carbon button electrode as the working electrode, a platinum wire as the auxiliary electrode, and a saturated calomel electrode (SCE) as the reference electrode. Tetrabutyl ammonium phosphorus hexafluoride (n-Bu_4NPF_6, 0.1 M) in acetonitrile was employed as the electrolyte, and the scan rate was set to be 100 mV s^{-1}. The SCE was calibrated using the ferrocene/ferrocenium (Fc/Fc^+) redox couple. Fc/Fc^+ is taken to be 4.8 eV relative to the vacuum level. [8]

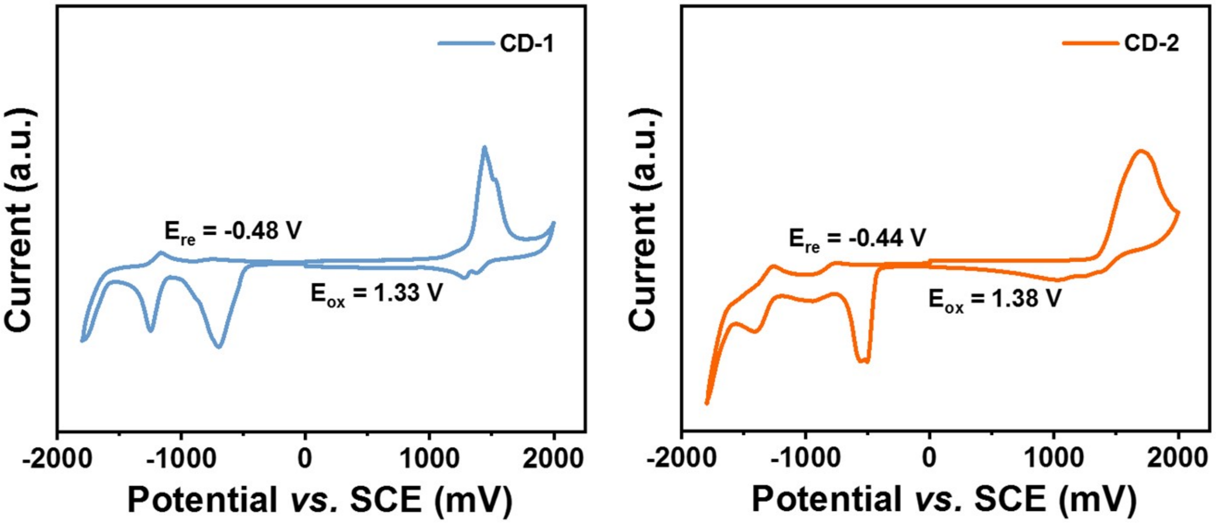

Figure S4. Oxidation/reduction scans of the acceptors.

5. UV-Vis and IR Spectroscopy

UV-Vis spectra in solution/film were recorded on a Cary 5000 UV-Vis spectrophotometer. The concentration of diluted solutions of acceptor was *ca.* 10^{-5} M. And the concentration of the solution for preparing the thin film of acceptor was *ca.* 15 mg mL^{-1}. The IR spectra of neat donor/acceptor powder were recorded on a NICOLET iS50 FT-IR spectrophotometer.

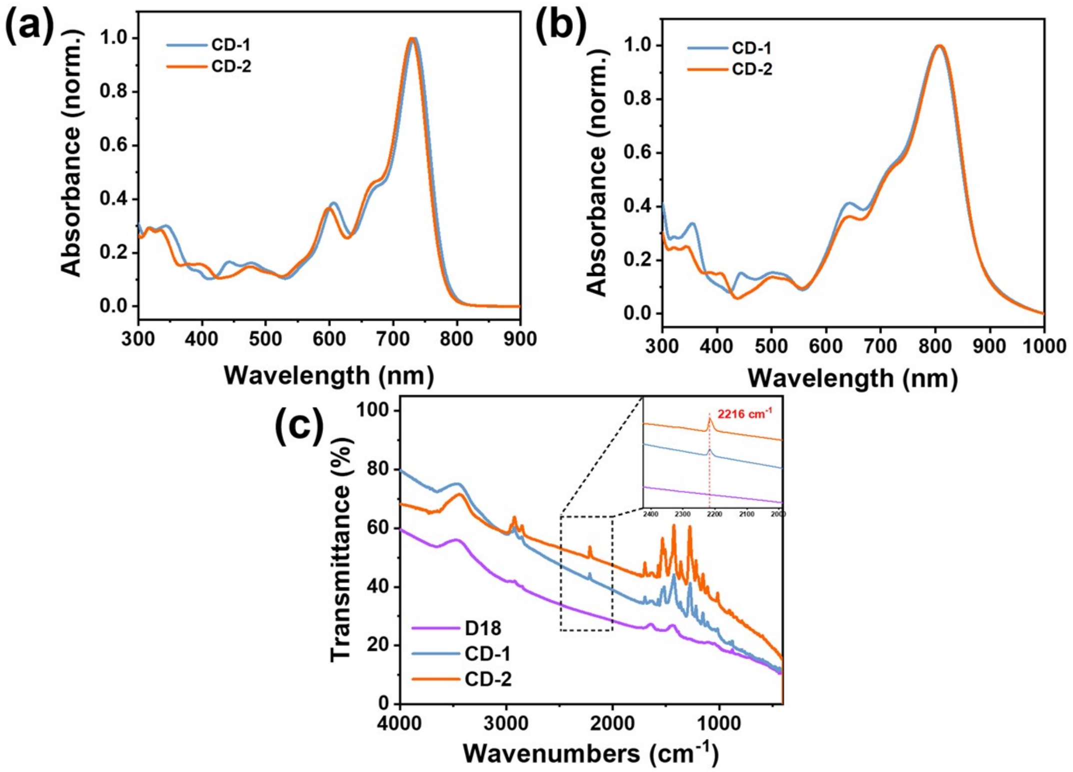

Figure S5. Normalized UV-vis spectra of acceptors in **(a)** chloroform solution and **(b)** in film. **(c)** The IR spectra of donor and acceptors neat film.

Table S2. The photophysical and electrochemical properties of Acceptors.

Molecule	λsol max (nm)	λfilm max nm)	Δλ (nm)	λfilm onset (nm)	Eox onset (V)	Ered onset (V)	Eopt gap[a] (eV)	LUMO[b] (eV)	HOMO[b] (eV)
CD-1	733	806	73	886	1.44	-0.48	1.40	-3.88	-5.69
CD-2	729	808	79	886	1.40	-0.44	1.40	-3.92	-5.74

[a] Eopt gap is derived from the absorption onset of the neat film of donor/acceptor: Eopt gap = 1240/λfilm onset;

[b] E_{HOMO} = -[Eox onset + (4.8 – $E_{Fc/Fc+}$)] eV; E_{LUMO} = -[Ered onset + (4.8 – $E_{Fc/Fc+}$)] eV.

6. Single Crystal X-ray Diffraction Experiments

The X-ray diffraction data was collected on a Bruker D8 VENTURE dual wavelength Mo/Cu diffractometer equipped with INCOATEC IμS DIAMOND CuKα radiation (λ= 0. 1.54178 Å) and a PHOTON III CMOS detector with a Helios Multi-layer Optic monochromator at 223 K temperature using an Oxford Cryosystems Cryostream 800 cryostat. All data collection was performed in shutterless mode, unit cell was determined by Bruker APEX5 software suite. The data sets were reduced and a multi-scan spherical absorption correction was implemented by Bruker SAINT v8.40B and SADABS-2016/2 in the SCALE interface.[9]

Structure was solved by intrinsic phasing method using the SHELXT 2018/2 and refined with full-matrix least squares on F^2 using the SHELXL 2019/3 by using OLEX2 1.5 as the graphical interface. Due to weak diffraction of the sample and the present of highly flexible carbon chains in the structure, DFIX, DANG instructions have been used to fix the flexible carbon chains in reasonable shape and positions, SIMU instruction to make the anisotropic displacement parameters of these carbon chains within reasonable limits. Unless otherwise stated, all non-hydrogen atoms in the structure were refined anisotropically and all hydrogen atoms were assigned isotropic displacement coefficients U(H) = 1.2 U or 1.5 U and their coordinates were allowed to ride on their respective atoms. In both cases the data quality is lower than ideal and the R factors higher than ideal due to the type of material being studied. However, the data are sufficient to confirm connectivity. In both cases the atoms in the chains have large adps due to unmodelled disorder. The solvent masking routine in Olex2 was used to mask the content from disordered solvent.[10-12] This was estimated to be two molecules of chloroform and 4 molecules of methanol per unit cell based on the experimental conditions used and electron density masked. The data for CD-2 were cut at 2 theta = 101 degrees as the high angle data had very low I/sigma such that they were essentially not present. The resolution is lower than ideal but sufficient to confirm the connectivity.

Table S3. Crystallographic parameters of CD-1 and CD-2.

	CD-1	**CD-2**
Empirical formula	$C_{99}H_{107}Cl_7N_8O_4S_4$	$C_{90}H_{94}Cl_4N_8O_2S_5$

Formula weight	1849.31	1621.83
Temperature/K	223.00	223.00
Crystal system	triclinic	monoclinic
Space group	P-1	C2/c
a/Å	10.5853(18)	29.131(5)
b/Å	21.091(4)	22.225(4)
c/Å	23.544(5)	14.008(2)
α/°	69.159(15)	90
β/°	81.645(13)	111.957(11)
γ/°	89.253(14)	90
Volume/Å^3	4856.1(17)	8412(2)
Z	2	4
ρ_{calc}g/cm^3	1.265	1.281
μ/mm^{-1}	3.094	2.851
F(000)	1944.0	3416.0
Crystal size/mm^3	0.13 × 0.11 × 0.09	0.12 × 0.1 × 0.09
Radiation	CuKα (λ = 1.54178)	CuKα (λ = 1.54178)
2Θ range for data collection/°	8.808 to 136.488	5.148 to 136.868
Index ranges	$-12 \leq h \leq 12$, $-25 \leq k \leq 25$, $-27 \leq l \leq 28$	$-32 \leq h \leq 34$, $-25 \leq k \leq 26$, $-16 \leq l \leq 16$
Reflections collected	66960	31882
Independent reflections	17739 [R_{int} = 0.0797, R_{sigma} = 0.0628]	7499 [R_{int} = 0.1004, R_{sigma} = 0.0944]
Data/restraints/parameters	17739/335/1031	7499/150/496
Goodness-of-fit on F^2	1.198	1.166
Final R indexes [I>=2σ (I)]	R_1 = 0.1078, wR_2 = 0.3004	R_1 = 0.1071, wR_2 = 0.2809

Final R indexes [all data]	$R_1 = 0.1436$, $wR_2 = 0.3403$	$R_1 = 0.1721$, $wR_2 = 0.3394$
Largest diff. peak/hole / e Å^{-3}	0.86/-1.37	0.76/-0.55

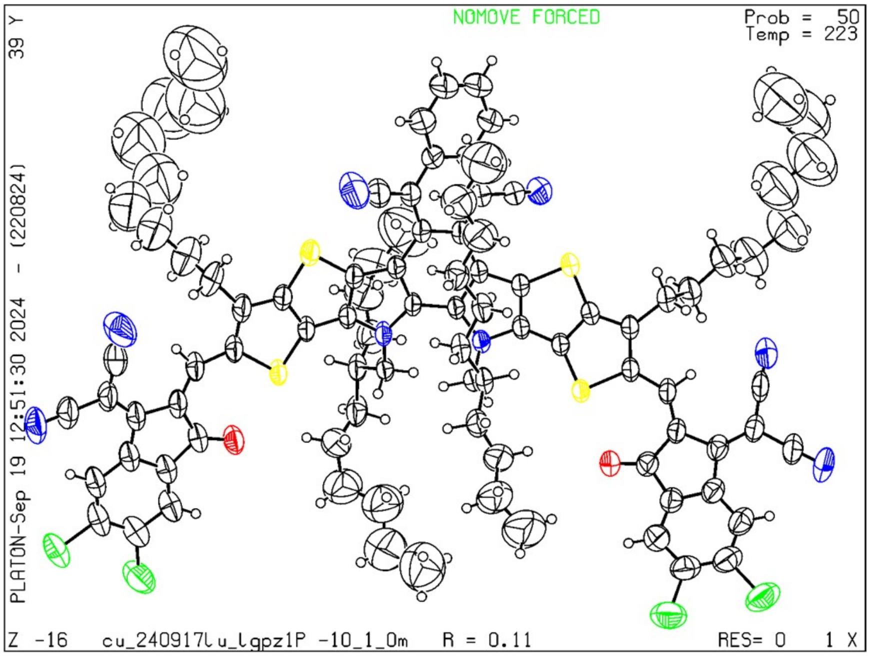

Figure S6. The ORTEP illustration with probability ellipsoids of **CD-1** (CCDC No. 2385866).

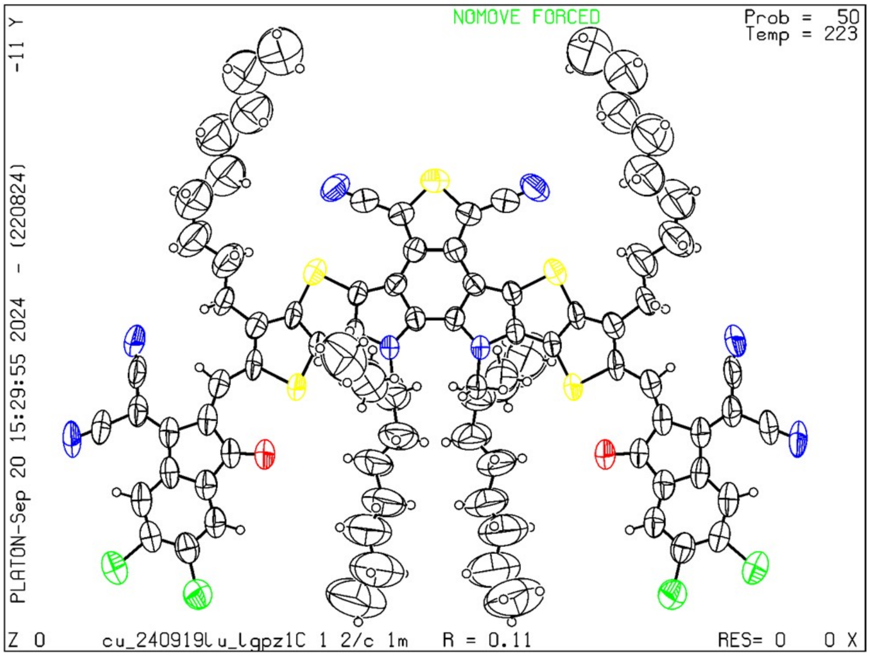

Figure S7. The ORTEP illustration with probability ellipsoids of **CD-2** (CCDC No. 2385867).

7. Device Fabrication and Characterizations

OFET devices

Thin film OFET devices: The bottom-gate bottom-contact (BG/BC) devices based on films of the two molecules CD-1 and CD-2 were fabricated with spin-coating process. The SiO_2/Si wafers with 300 nm thermally grown SiO_2 ($Ci \approx 11.5$ nF cm^{-2}) were used as substrates. Firstly, the substrates were rinsed with deionized water, hot piranha solution ($H_2SO_4/H_2O_2 = 2:1$), deionized water, ethanol, respectively. For the vapor-based OTS modification, the petri dish was put into a vacuum oven and kept at 120 °C for 3 hours. When the temperature returned to room temperature, OTS-self-assembled monolayer was formed on the surface of the substrates. Those OTS modified wafers should be washed successively by hexane, ethanol, and chloroform and blown dry with high-purity nitrogen gas before use. The BGBC devices were fabricated by spin-coating. Prior to the semiconductor layer deposition, Au electrodes were sputtered and patterned onto the SiO_2/Si wafers by photolithography technique, acting as source and drain electrodes ($L/W = 20/1400$). In order to decrease the contact resistance, the photolithography process was carried out before the OTS modification process. The CD-1 and CD-2 solutions were spun in N_2 with a speed of 1500 rpm for 60 s to obtain the semiconductor layers. The devices were annealed in a vacuum oven at 150 °C for 20 min in a nitrogen (N_2)-filled glove box before measurements.

Single crystal OFET devices: The bottom-gate top-contact (BG/TC) devices based on the single-crystals of CD-1 and CD-2 growing on the SiO_2/Si substrates were fabricated with the “gold strips” method to investigate their charge transport properties. The SiO_2/Si wafers used to grow crystals were first cleaned with hot piranha solution ($H_2SO_4/H_2O_2 = 2:1$) followed by a copious rinsing with deionized water and finally were blown dry by nitrogen gun. Single crystals of CD-1 and CD-2 were synthesized via drop-casting their chlorobenzene solution (0.2 mg/mL), onto SiO_2/Si substrates in a sealed bottle under typical growth conditions at room temperature. The solvent was controlled to slowly evaporate in several days. Then the single crystals in micrometer scale may grow on the substrates. The best quality crystals were selected on a micromanipulator station coupled with an optical microscope to further fabricate the transistor devices. Two Au films, approximately 150 μm × 30 μm, were glued onto the selected single crystals via the electrostatic forces with the help of the S8mechanical probes in the Micromanipulator. The abovementioned

Au films were prepared as follows: Firstly, a patterned Au thin film with a thickness around 100 nm was pre-deposited on a Si wafer by thermal evaporation with a copper mask. Then, two small pieces of the Au films with desired sizes were peeled off from the Si substrate with the tip of the mechanical probe and transferred onto the single crystals as source and drain electrodes. The Si substrate functioned as the gate electrode.

The electrical properties of OFETs were measured using a semiconductor parameter analyzer (Platform Design Automation FS380 Pro) in glove box with nitrogen atmosphere. The charge mobility was extracted from the saturation regime and calculated from the following equation:

$$I_{DS} = \frac{W}{2L} C_i \mu (V_{GS} - V_T)^2$$

Where I_{DS} is the drain-source current, μ is the field-effect mobility W/L is the channel width/length, C_i is the capacitance per unit area of gate dielectric layer, and V_G and V_T are the gate voltage and threshold voltage, respectively.

OSC devices

The conventional devices were fabricated with an architecture of ITO/3-BPIC-F/D18:acceptor/PNDIT-F3N[13]/Ag. Firstly, the ITO glass was pre-cleaned sequentially in an ultrasonic bath of detergent, deionized water, acetone and isopropanol. Then the surface of ITO was treated by UV light in an ultraviolet-ozone chamber (Jelight Company) for 15 min. Afterwards, A thin layer of 3-BPIC-F was deposited on the ITO substrate at 3000 rpm for 20 s and then dried at 100 °C for 10 mins in air.[1] Then the substrates were transferred to a glovebox filled with nitrogen. Then the D18:CD-1 (1:1 w/w) and D18:CD-2 (1:0.8 w/w), were dissolved chloroform (CF) at the concentration of 4 mg/mL of D18. All the solutions need to be stirred at 100 °C for 2 hours. Then the resulting solutions were spin-casted at 2000 rpm for 20 s onto the 3-BPIC-F layer. And then the films were treated with the thermal annealing (TA) at 100 °C for 10 min. After that, a thin layer of PNDIT-F3N (dissolved in methanol with the concentration of 1 mg/mL) was spin-coated on the top of the active layer. Finally, a layer of Ag with thickness of 150 nm was deposited under 2×10^{-6} Pa. The active area of the device was *ca.* 4 mm^2, and a shadow mask with defined area of 3.24 mm^2 was used during the testing.

The current density-voltage (*J*-V) curves of the prepared photovoltaic devices were recorded by a Keithley 2400 source-measure unit. The photocurrent was measured under the simulated illumination of 100 mW cm^{-2} with AM1.5 G using a Enli SS-F5-3A solar simulator, which was calibrated by a standard Si solar cell (made by Enli Technology Co., Ltd., Taiwan, and calibrated report can be traced to NREL). The thickness of the active layers was measured by a Veeco Dektak 150 profilometer. The EQE spectra were recorded by using a QE-R Solar Cell. Response Measurement System (Enli Technology Co., Ltd., Taiwan).

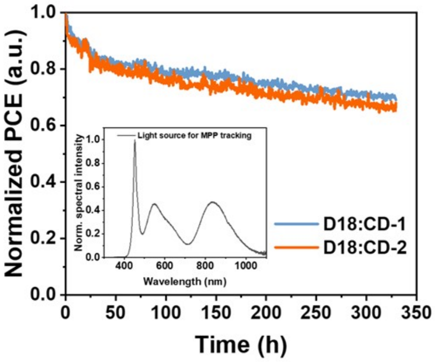

Figure S8. Normalized PCE expressed as a function of light-soaking time under MPP tracking.

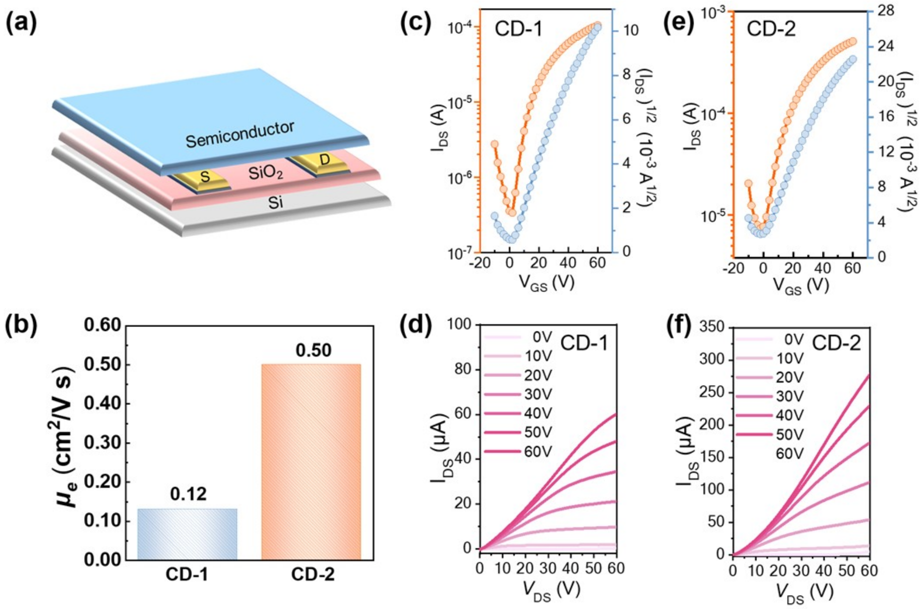

Figure S9. (a) Architecture of the solution processed OFET device. (b) Maximum electron mobility extracted from 20 transistor devices. (c) Typical transfer and (d) output curves of the CD1-based OFETs. (e) Typical transfer and (f) output curves of the CD2-based OFETs.

Table S4. Device optimization of **D18:CD-1** based binary system.

D:A ratio (m/m)	Post-treatment	V_{OC} (V)	J_{SC} (mA cm^{-2})	FF (%)	PCE (%)
1:0.8	100 °C 8 mins	0.934	25.77	77.1	18.7
1:1		0.940	26.54	78.4	19.6
1:1.2		0.940	26.39	77.7	19.3

Table S5. Device optimization of **D18:CD-2** based binary system.

D:A ratio (m/m)	Post-treatment	V_{OC} (V)	J_{SC} (mA cm^{-2})	FF (%)	PCE (%)
1:0.7	100 °C 8 mins	0.887	26.99	78.4	18.7
1:0.8		0.889	26.74	80.3	19.1
1:1		0.881	26.92	77.2	18.3

8. E_{loss} Analysis

The following equation was used to quantify the E_{loss} of OSCs:

$$E_{\text{loss}} = E_{\text{g}}^{\text{PV}} - qV_{\text{oc}} = \left(E_{\text{g}}^{\text{PV}} - qV_{\text{oc}}^{\text{SQ}}\right) + \left(qV_{\text{oc}}^{\text{SQ}} - qV_{\text{oc}}^{\text{rad}}\right) + \left(qV_{\text{oc}}^{\text{rad}} - qV_{\text{oc}}\right) = \Delta E_1 + \Delta E_2 + \Delta E_3$$

*E*PV g represents the bandgap of the blend film and *q* is the elementary charge. *E*PV g can be estimated via the derivatives of the sensitive EQE (EQE_{PV}) spectra(P(E)=*d*EQE/*d*E) as following:

$$E_{\text{g}}^{\text{PV}} = \frac{\int_a^b E_{\text{g}} \text{P}(E_{\text{g}}) \text{d}E_{\text{g}}}{\int_a^b \text{P}(E_{\text{g}}) \text{d}E_{\text{g}}}$$

where the integration limits *a* and *b* are chosen as the energy where $\text{P}(E_{\text{g}})$ is equal to 50% of its maximum, as exemplarily depicted in **Figure S9**. The EQE_{PV} measurements were conducted on an Enlitech FTPS PECT-600 instrument. The total E_{loss} can be divided into three parts:

(1) $\Delta E_1 = E_g - qV_{\text{oc}}^{\text{SQ}}$ represents the unavoidable radiative loss originating from absorption above the bandgap. The $V_{\text{oc}}^{\text{SQ}}$ is the maximum voltage based on the Shockley–Queisser (SQ) limit:

$$V_{\text{oc}}^{\text{SQ}} = \frac{kT}{q} \ln\left(\frac{J_{\text{sc}}^{\text{SQ}}}{J_0^{\text{SQ}}} + 1\right) \cong \frac{kT}{q} \ln\left(\frac{q \cdot \int_{\boldsymbol{E}_{\text{g}}}^{+\infty} \phi_{\text{AM1.5G}}(E) \text{d}E}{q \cdot \int_{\boldsymbol{E}_{\text{g}}}^{+\infty} \phi_{\text{BB}}(E) \text{d}E}\right)$$

(2) $\Delta E_2 = qV_{\text{oc}}^{\text{SQ}} - qV_{\text{oc}}^{\text{rad}}$ can be regarded as radiative loss caused by absorption below the bandgap, where the $V_{\text{oc}}^{\text{rad}}$ is the open circuit voltage when there is only radiative recombination. The radiative recombination limit for the saturation current (J_0^{rad}) is also calculated from the EQE spectrum:

$$V_{\text{oc}}^{\text{rad}} = \frac{kT}{q} \ln\left(\frac{J_{\text{sc}}}{J_0^{\text{rad}}} + 1\right) \cong \frac{kT}{q} \ln\left(\frac{q \cdot \int_0^{+\infty} \text{EQE}(E) \phi_{\text{AM1.5G}}(E) \text{d}E}{q \cdot \int_0^{+\infty} \text{EQE}(E) \phi_{\text{BB}}(E) \text{d}E}\right)$$

where q is the elementary charge and ϕ_{BB} is the black body spectrum at 300 K.

(3) $\Delta E_3 = qV_{\mathrm{oc}}^{\mathrm{rad}} - qV_{\mathrm{oc}}$ can be directly calculated while the other two parts were determined. ΔE_3 can also be confirmed by measuring the EQE of electroluminescence ($\mathrm{EQE_{EL}}$) of the solar cell through the equation of: $\Delta E_3 = -kT\ln\left(\mathrm{EQE_{EL}}\right)$. For the $\mathrm{EQE_{EL}}$ measurements, a digital source meter (Keithley 2400) was 80 employed to inject electric current into the solar cells, and the emitted photons were collected by a Si diode (Hamamatsu s1337-1010BQ) and indicated by a picoammeter (Keithley 6482).

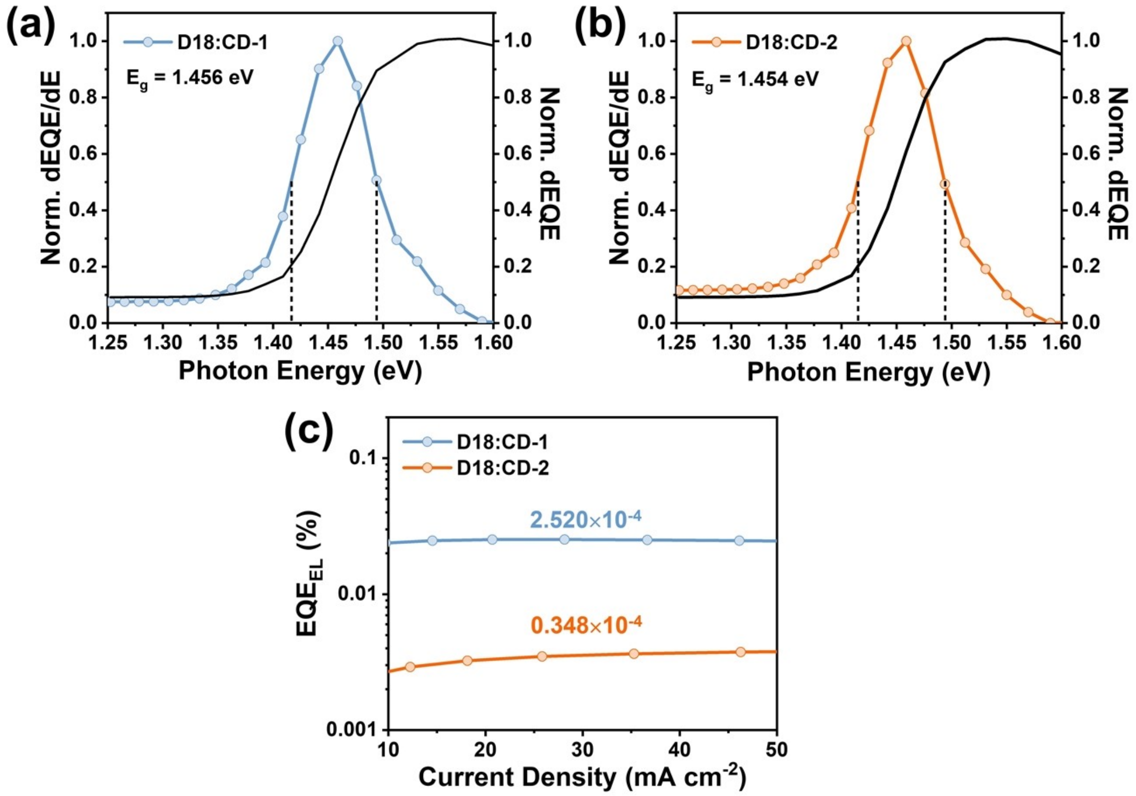

Figure S10. (a, b) Optical bandgap determination of blend films on the basis of the derivatives of the sensitive EQE spectra for optimized OSCs. (c) The $\mathrm{EQE_{EL}}$ spectra for the optimized devices.

Table S6. Detailed distributions of total energy loss in OSCs based on the SQ limit theory.

Blend	***E*PV g (eV)**	***V*SQ OC (V)**	**ΔE_1 (eV)**	***V*rad OC (V)**	**ΔE_2 (eV)**
D18:CD-1	1.456	1.188	0.268	1.124	0.064
D18:CD-2	1.454	1.186	0.268	1.125	0.061

Blend	**ΔE_3 (eV)[a]**	**EQE_{EL} (10^{-4})**	**ΔE_3 (eV)[b]**	**V_{oc} (V)**	**E_{loss} (eV)**
D18:CD-1	0.184	2.520	0.214	0.940	0.516
D18:CD-2	0.236	0.348	0.265	0.889	0.565

[a] Calculated from the *V*SQ OC through the equation of: $\Delta E_3 = qV$rad OC − qV_{OC};

[b] Calculated from the EQE_{EL} through the equation of: $\Delta E_3 = -kT\ln(EQE_{EL})$.

9. Urbach Energy Measurements

The Urbach energy (E_u) of binary devices was evaluated by measuring the fourier transform photocurrent spectroscopy-external quantum efficiency (FTPS-EQE).

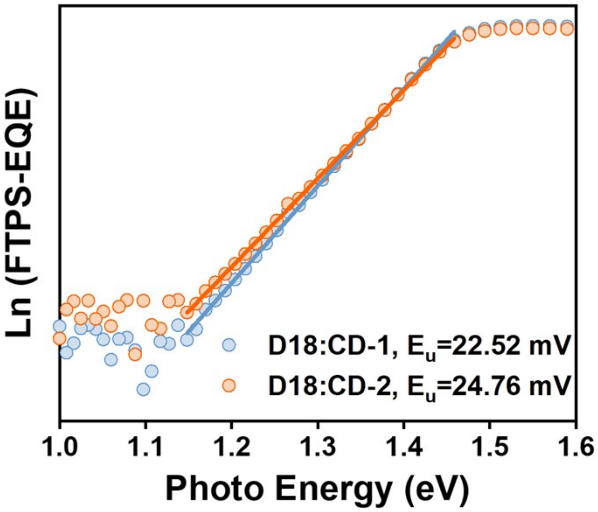

Figure S11. The Urbach energy of binary devices.

10. Charge Carrier Mobility Measurements

The carrier mobility (hole and electron mobility) of photoactive active layer was obtained by fitting the dark current of hole/electron-only diodes to the space-charge-limited current (SCLC) model. Hole-only diode configuration: Glass/ITO/3-BPIC-F/active layer/MoO_3/Ag; Electron-only diode configuration: Glass/ITO/ZnO/active layer/PNDIT-F3N/Ag. The SCLC mobility was estimated using the following equation:

$$J = \frac{9\varepsilon_r \varepsilon_0 \mu V^2}{8L^3}$$

where J is the current density, ε_r is the dielectric permittivity of the active layer, ε_0 is the vacuum permittivity, L is the thickness of the active layer, μ is the hole/electron mobility.

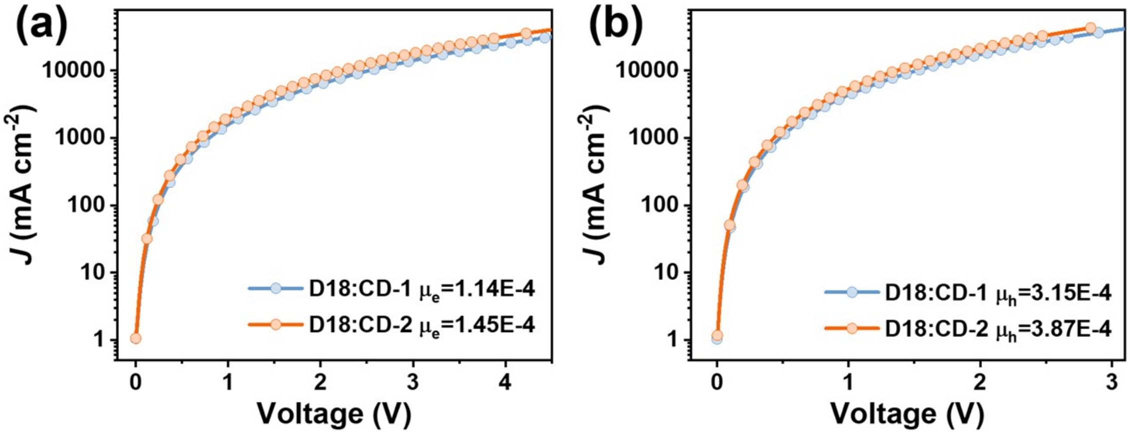

Figure S12. (a) Electron and (b) hole mobility of optimized devices.

Table S7. Average mobility values of optimized devices.

Blend	**μ_e ($\times10^{-4}$ cm^2/Vs)**	**μ_h ($\times10^{-4}$ cm^2/Vs)**	**μ_h/μ_e**
D18:CD-1	1.14	3.15	2.76
D18:CD-2	1.45	3.87	2.67

11. Charge Carrier Recombination Analysis

In OSCs, bimolecular recombination and trap-assisted recombination are the two major charge carrier recombination channels that would result in the loss of PCEs. To probe how these recombination losses affect the device performances, *J–V* characteristics under different light intensities were measured. To quantify the bimolecular recombination rate, the relationship between J_{SC} and light intensity was investigated. According to previous reports, J_{SC} and incident light intensity (I) show a power-law dependence of $J \propto I^{\alpha}$, where α represents the power factor. The bimolecular recombination efficiency (η) then can be quantified as $\eta = 1/\alpha - 1$, which means the closer the α is to 1, the more unlikely bimolecular recombination occurs. Similarly, the trap-assisted recombination can be recorded by monitoring the relationship between V_{OC} and light intensity. Usually, V_{OC} and the natural logarithm of I are related by $V_{OC} \propto n(kT/q)\ln(I)$, where k, T, and q represent the Boltzmann constant, temperature in Kelvin, and elementary charge, respectively. The value of n ranges from 1 to 2, and n equal to unity indicates trap-free conditions. Any deviation from 1 indicates that charge-carrier traps exist to a certain degree in the active layer or the interface between the active layer and the electrode in the device.

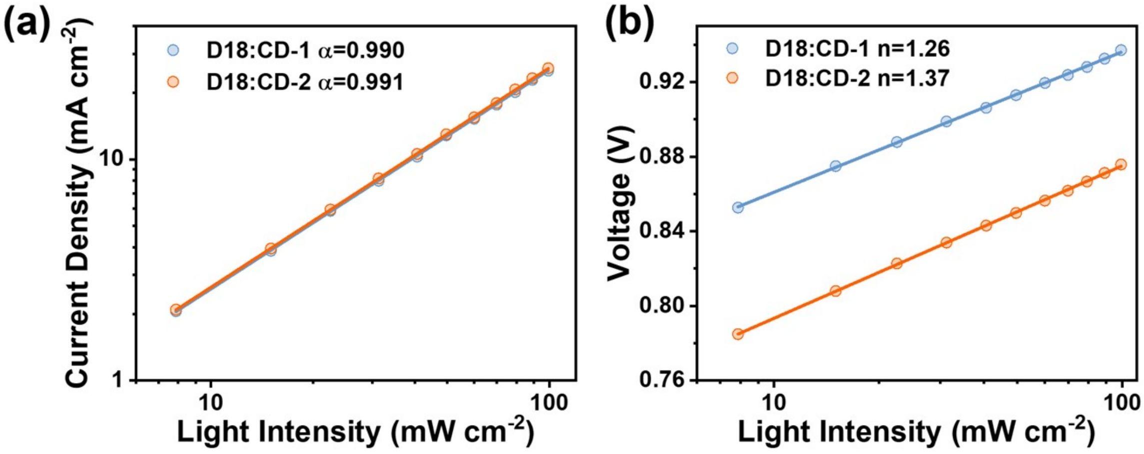

Figure S13. (a) J_{SC} and (b) V_{OC} *vs.* light intensity for optimized for optimized device.

12. Transient photocurrent/photovoltage (TPC/TPV) Characterization

Transient photocurrent (TPC) and photovoltage (TPV) measurements were performed on a Molex 180081-4320 with light intensity about 0.5 sun, Voltage and current dynamics were recorded on a digital oscilloscope (Tektronix MDO4104C). Voltages at open circuit and currents under short circuit conditions were measured over a 1 MΩ and a 50 Ω resistor, respectively.

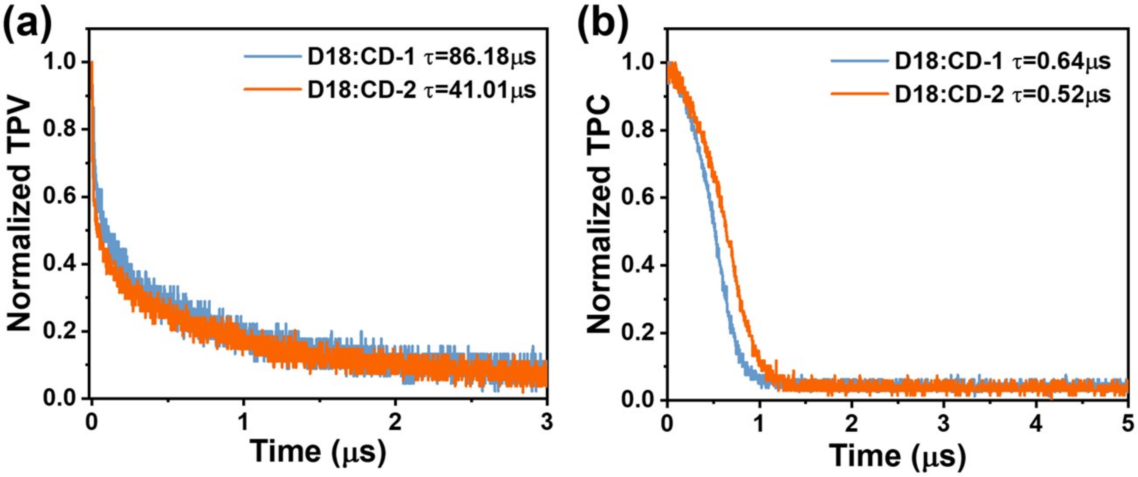

Figure S14. TPV and TPC diagram of optimized OSC devices.

13. Grazing-Incidence Wide-Angle X-ray Scattering (GIWAXS)

Si substrates were sonicated for 15 min in turn in successive baths of acetone and isopropanol. The substrates were then dried with pressurized nitrogen before being exposed to the UV-ozone plasma for 15 min. Then the samples were prepared by following methods described in Section 7. "Device Fabrication and Characterizations".

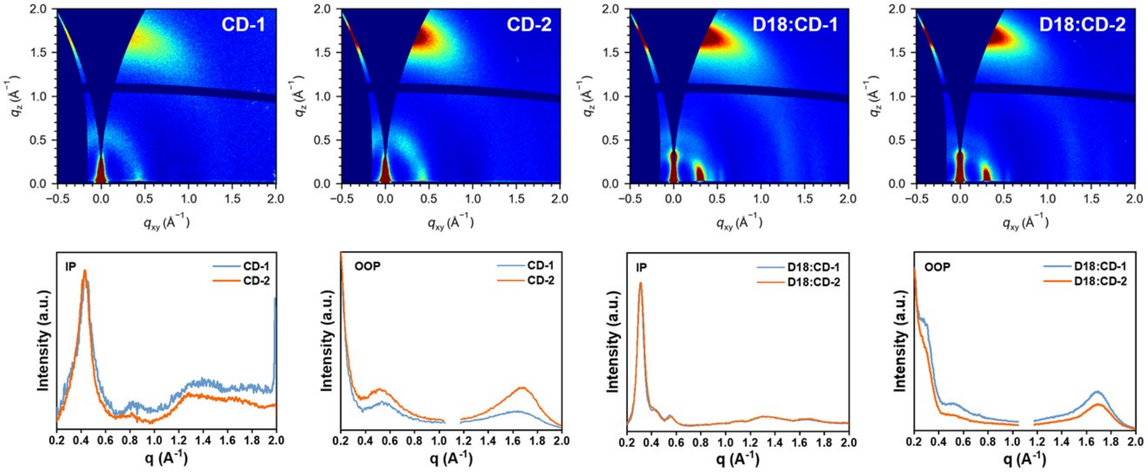

Figure S15. 2D GIWAXS patterns and in-plan/out-of-plane line-cut profiles of films.

Table S8. Crystallographic parameters of GIWAXS scattering profiles.

Materials	Lattice plane	Peak location (Å^{-1})	d-spacing(Å)	FWHM(Å^{-1})	CL(Å)
CD-1	010 (OOP)	1.643	3.822	0.575	9.830
	100 (IP)	0.430	14.605	0.137	41.255
CD-2	010 (OOP)	1.667	3.767	0.295	19.159
	100 (IP)	0.433	14.503	0.106	53.321
D18:CD-1	010 (OOP)	1.688	3.720	0.244	23.164
	100 (IP)	0.310	20.258	0.049	115.347
D18:CD-2	010 (OOP)	1.707	3.679	0.236	23.949
	100 (IP)	0.310	20.258	0.052	108.692

14. Contact Angles Measurements

The contact angles of two different solvents (water and glycerol) on the neat films (donor/acceptor) were measured on a JC2000D1 drop shape analyzer (POWEREACH®). The miscibility of two components in the blend can be estimated from the solubility parameters (δ) of each material, which can be calculated with equation: $\delta = K\sqrt{\gamma}$, Where γ is the surface energy of the material, and K is the proportionality constant ($K = 116 \times 10^3$ $m^{1/2}$).

Figure S16. Contact angle images of water and glycerol droplets on the neat films.

Table S9. Contact angle of neat films and miscibility parameters

Materials	H_2O (θ_1)	Gly (θ_2)	Surface free energy γ (mN m-1)	$\chi_{donor-acceptor}$ (k)
D18	105.51	91.77	19.80	\
CD-1	94.09°	87.84°	17.16	0.094
CD-2	93.79°	87.48°	17.37	0.079

15. Solution NMR Spectra

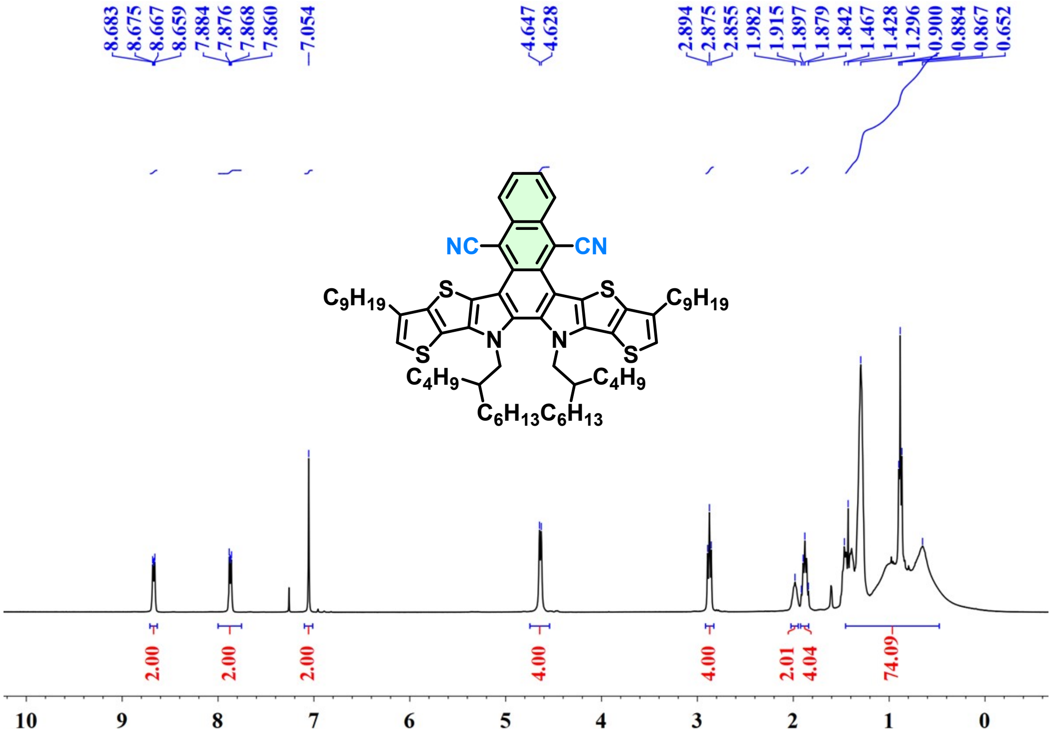

Figure S17. ^{1}H NMR spectrum of compound **2** in $CDCl_3$

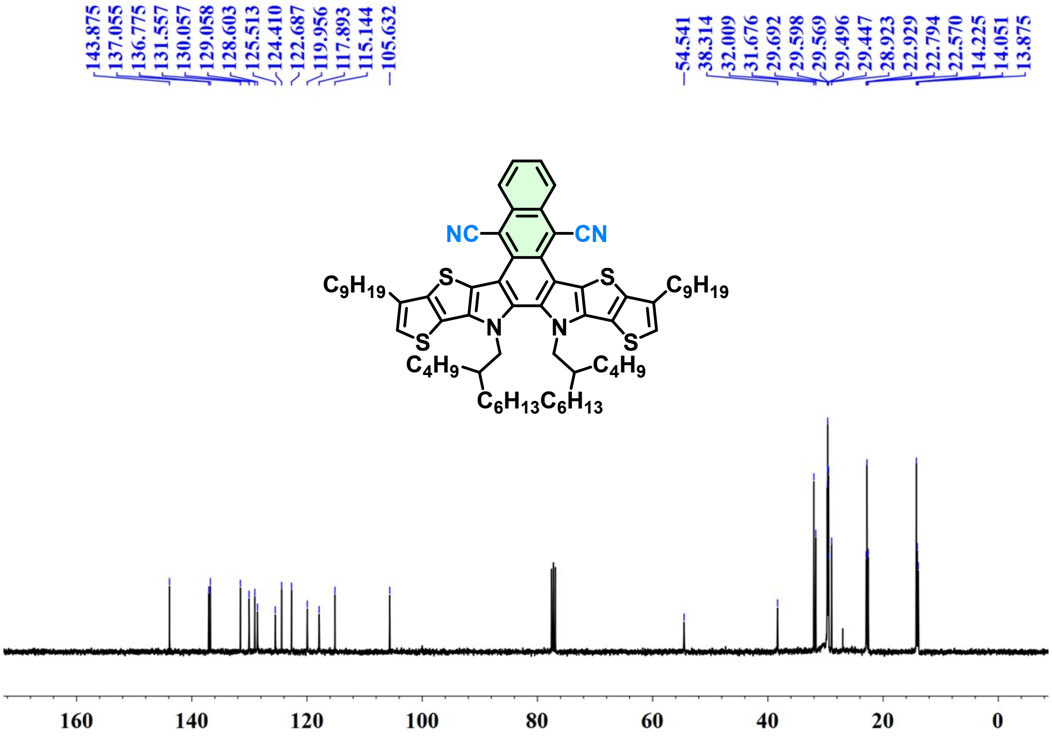

Figure S18. ^{13}C NMR spectrum of compound **2** in $CDCl_3$

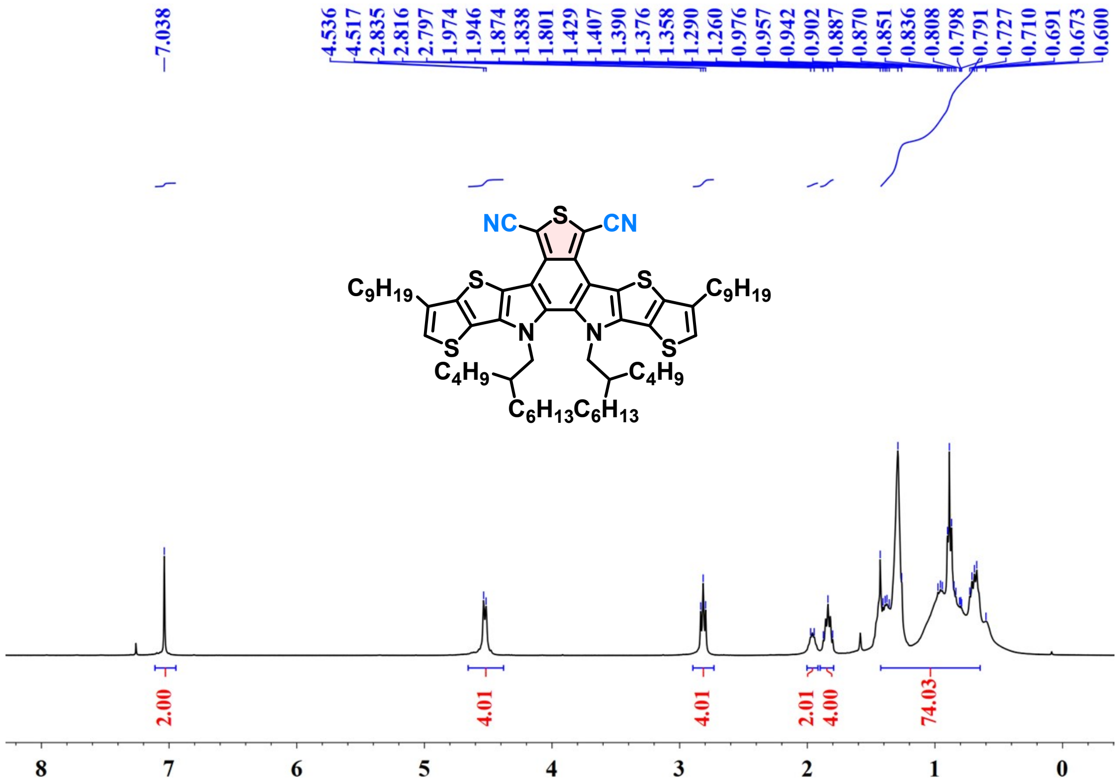

Figure S19. ^{1}H NMR spectrum of compound **3** in $CDCl_3$

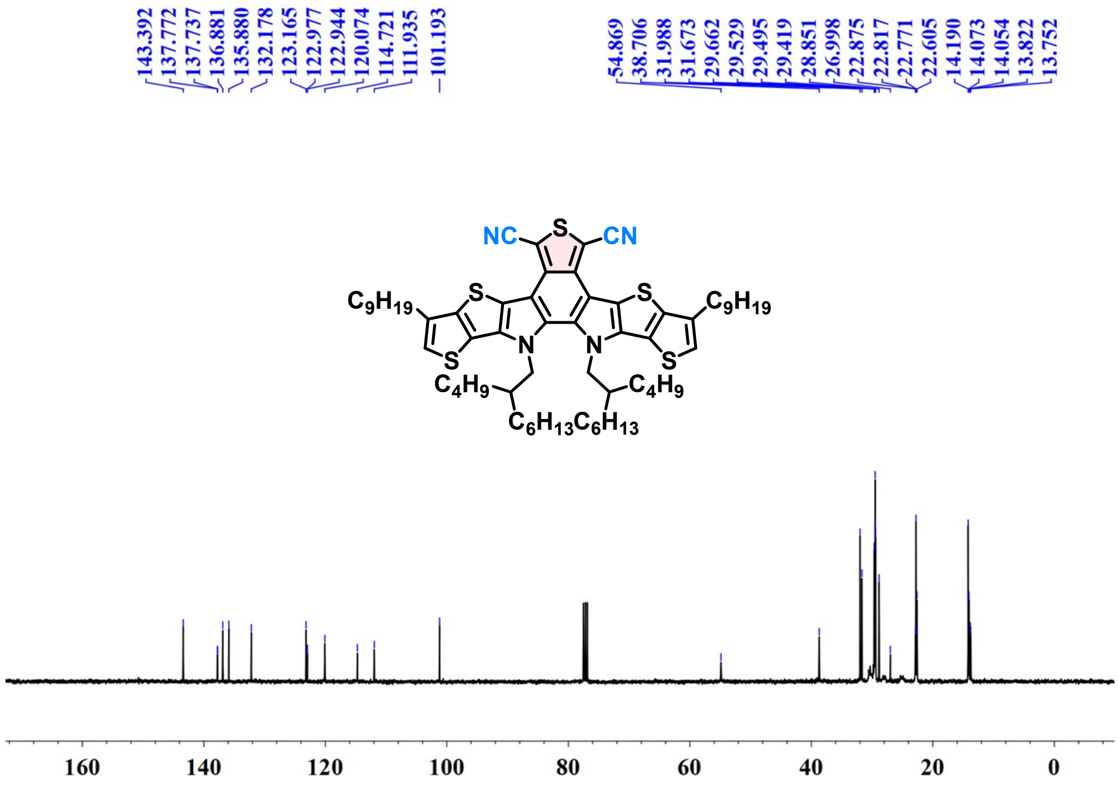

Figure S20. ^{13}C NMR spectrum of compound **3** in $CDCl_3$

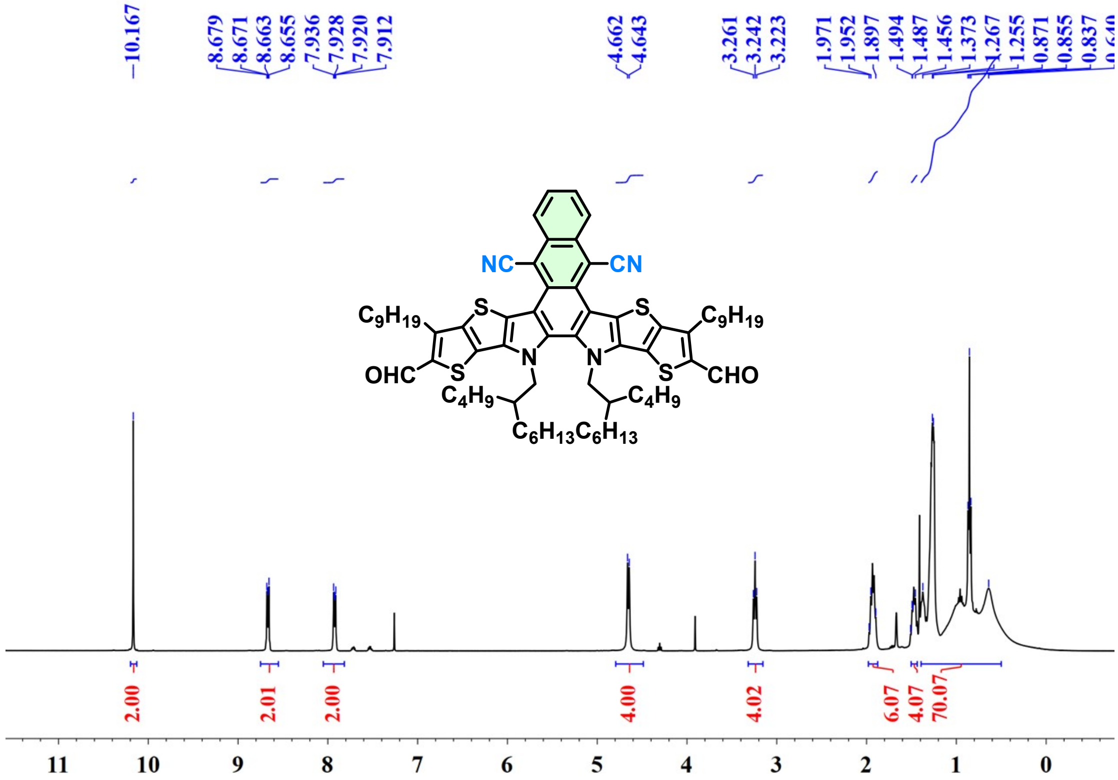

Figure S21. ^1H NMR spectrum of compound **4** in $CDCl_3$

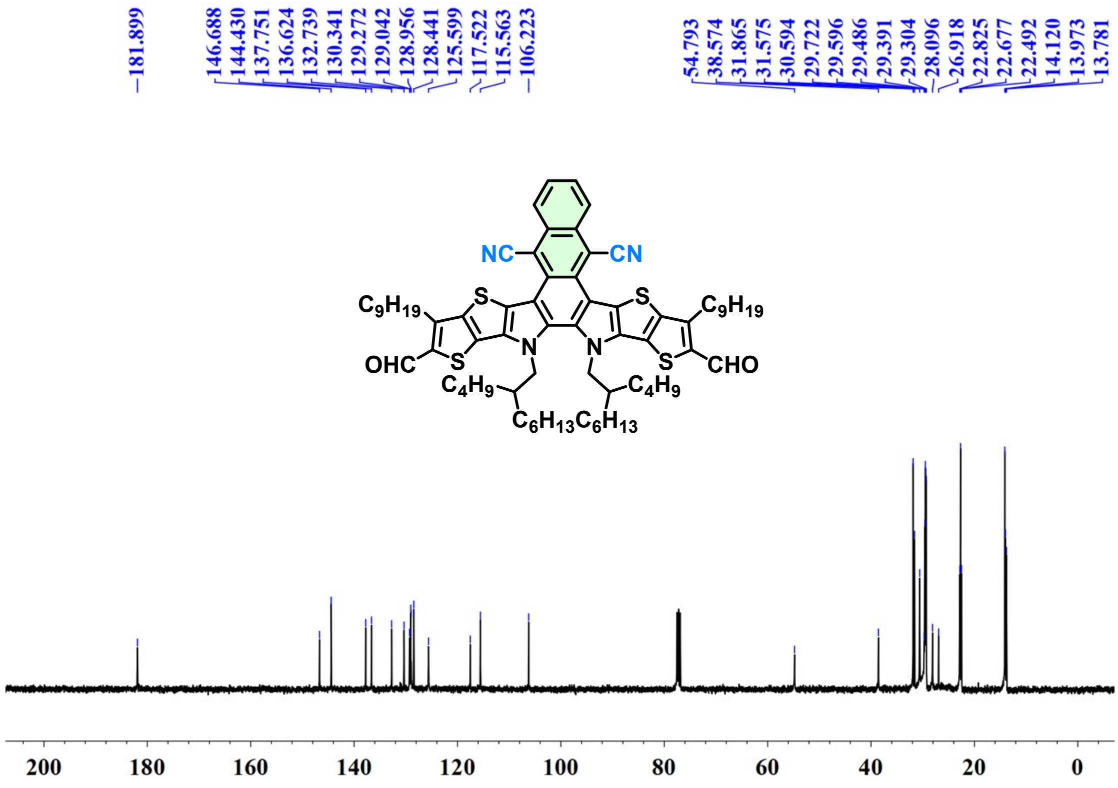

Figure S22. ^{13}C NMR spectrum of compound **4** in $CDCl_3$

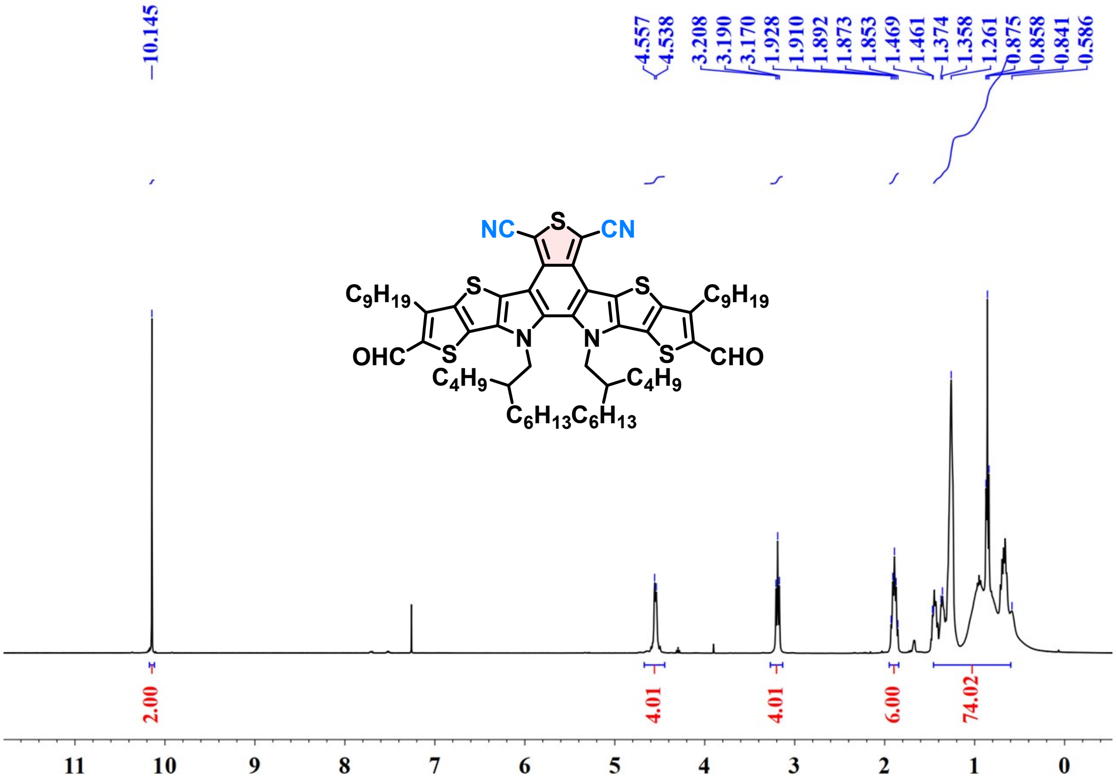

Figure S23. ^{1}H NMR spectrum of compound **5** in CDCl$_3$

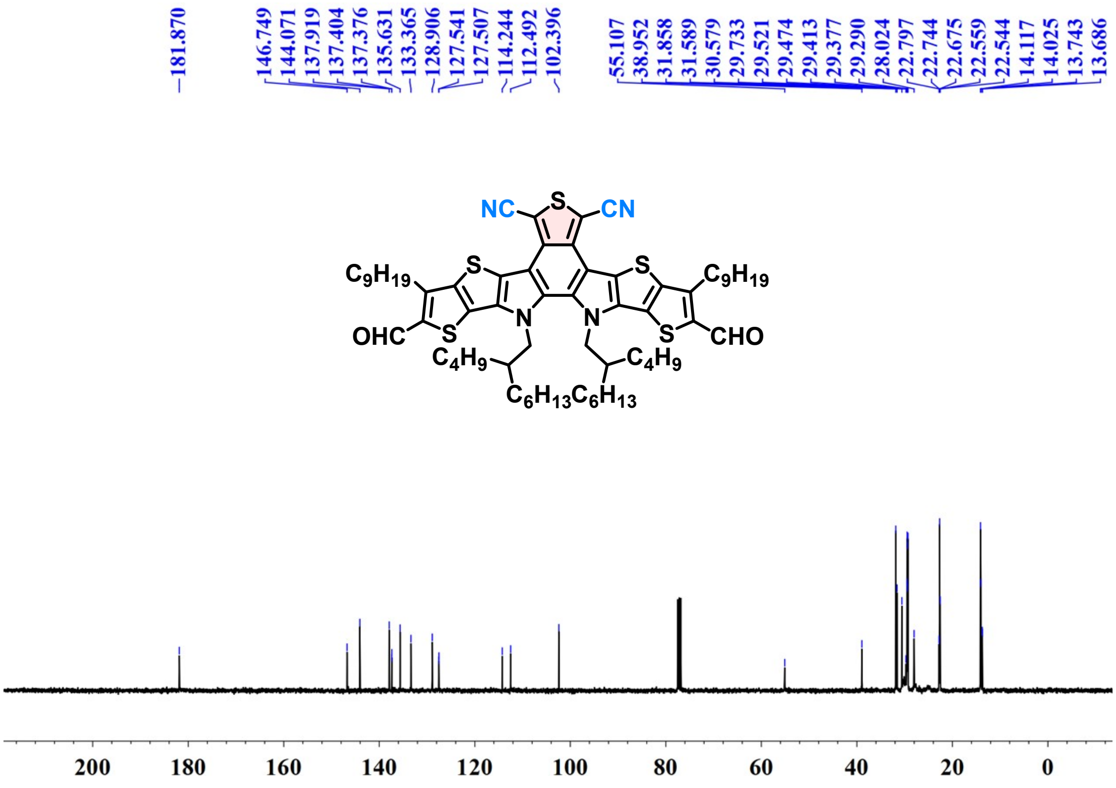

Figure S24. ^{13}C NMR spectrum of compound **5** in CDCl$_3$

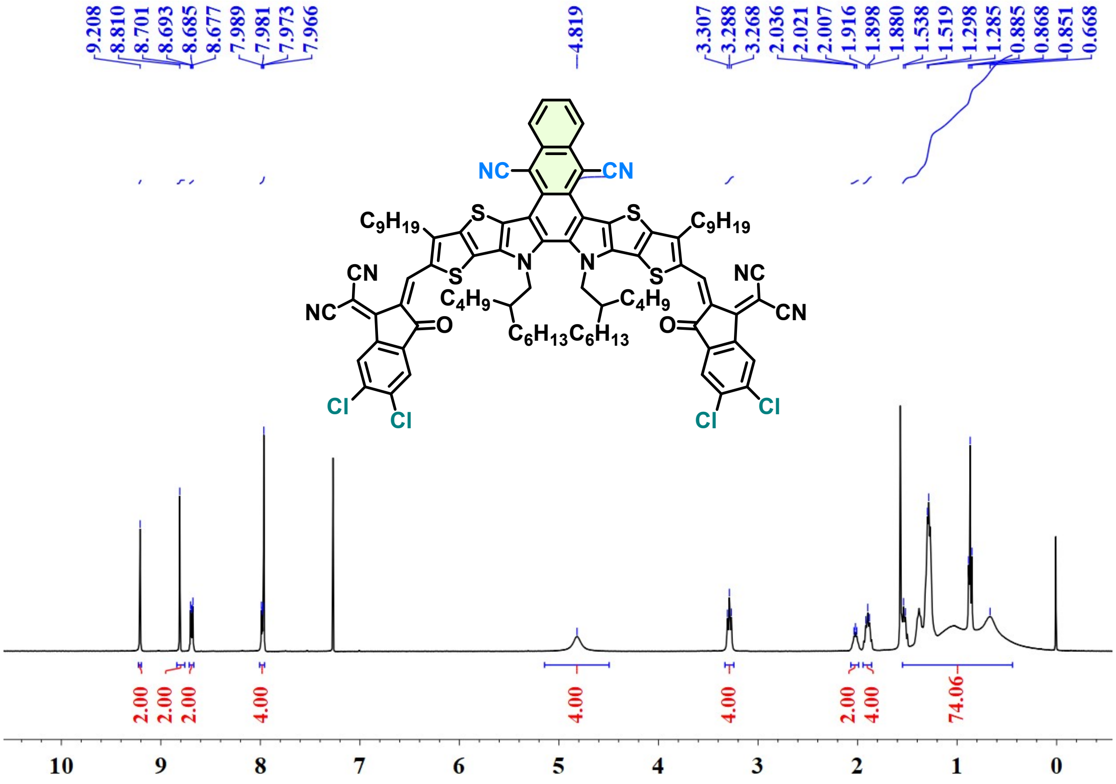

Figure S25. ^{1}H NMR spectrum of compound **CD-1** in $CDCl_3$

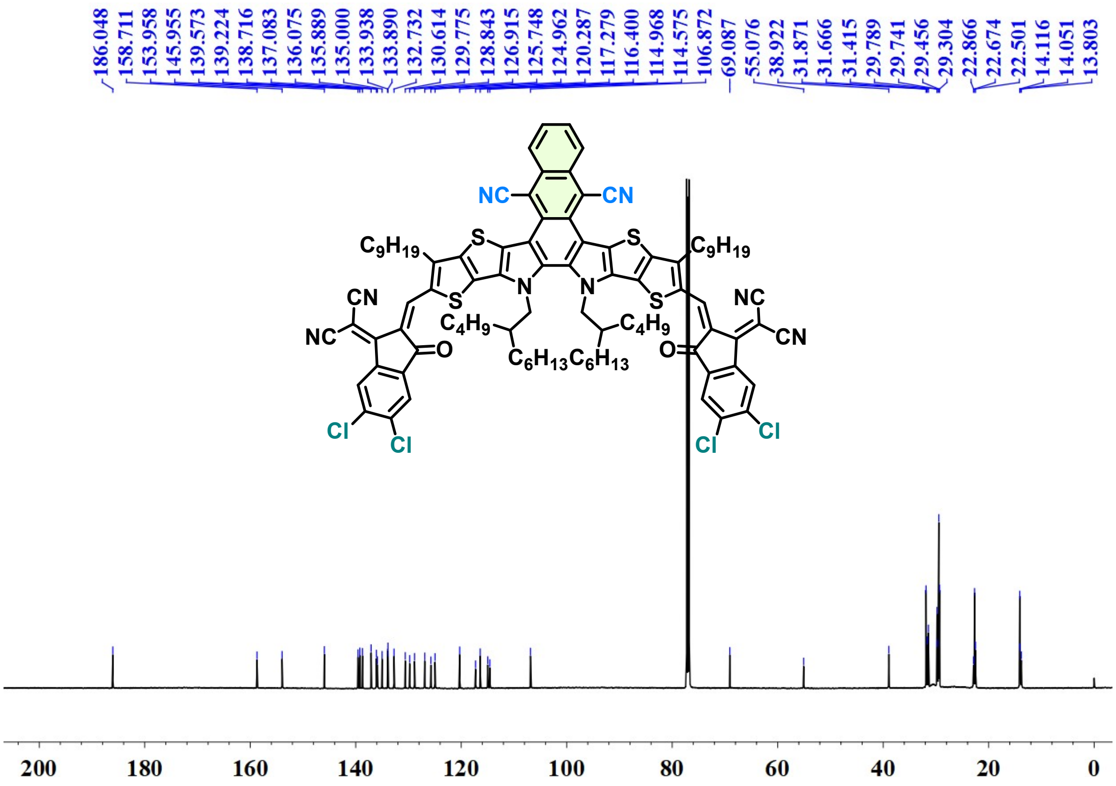

Figure S26. ^{13}C NMR spectrum of compound **CD-1** in $CDCl_3$

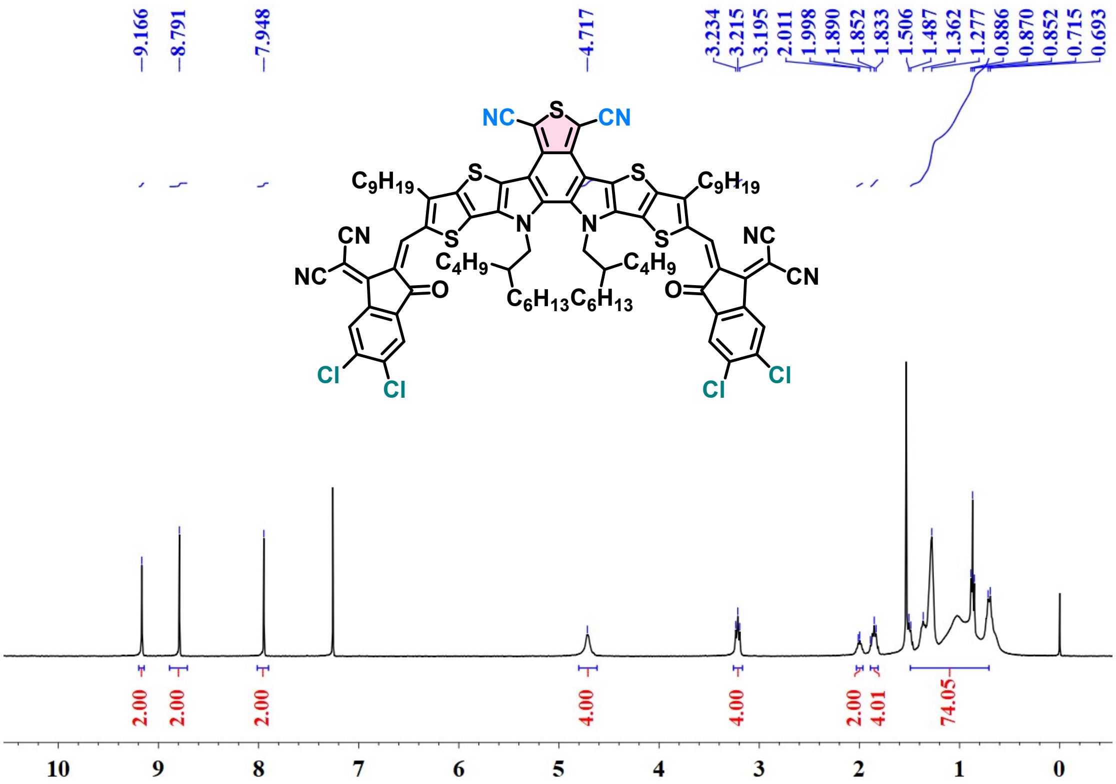

Figure S27. ^{1}H NMR spectrum of compound **CD-2** in $CDCl_3$

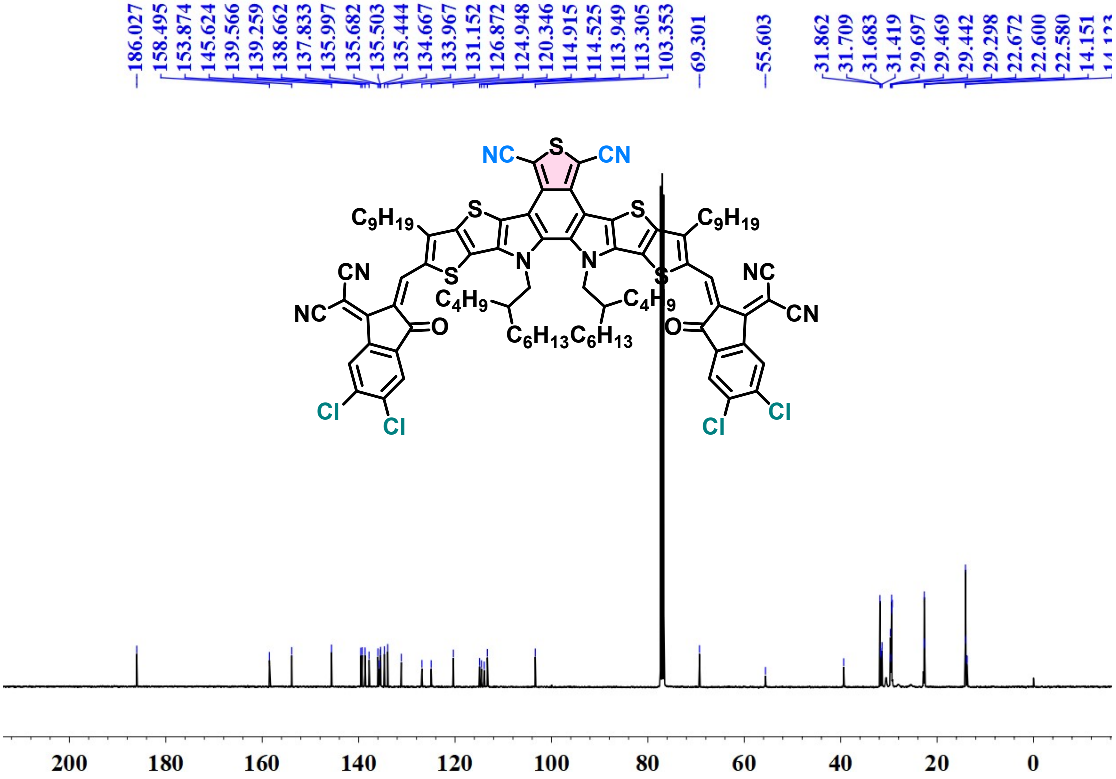

Figure S28. ^{13}C NMR spectrum of compound **11** in $CDCl_3$

16. High-Resolution Mass Spectra

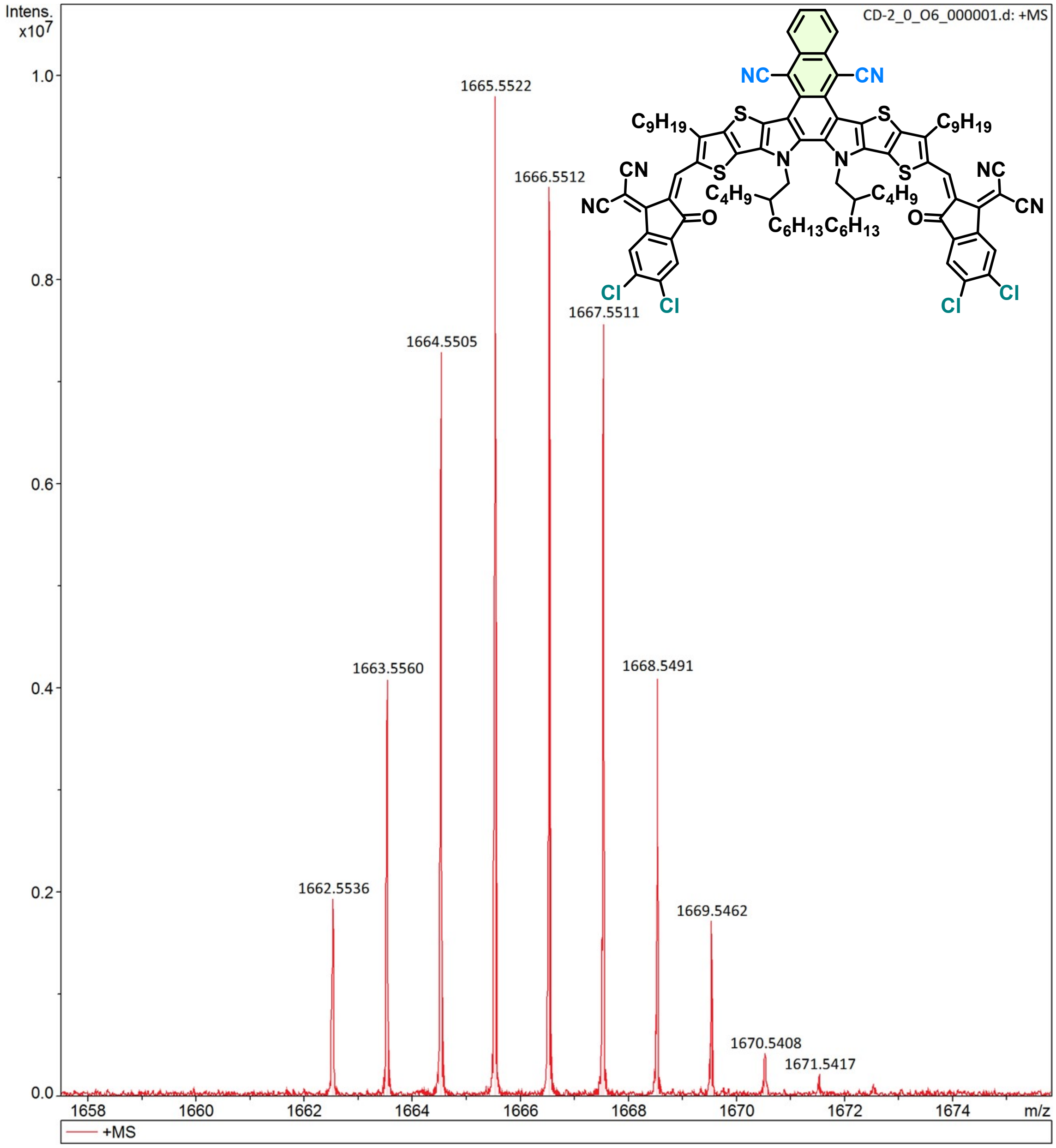

Figure S29. HR-MS spectrum of **CD-1**

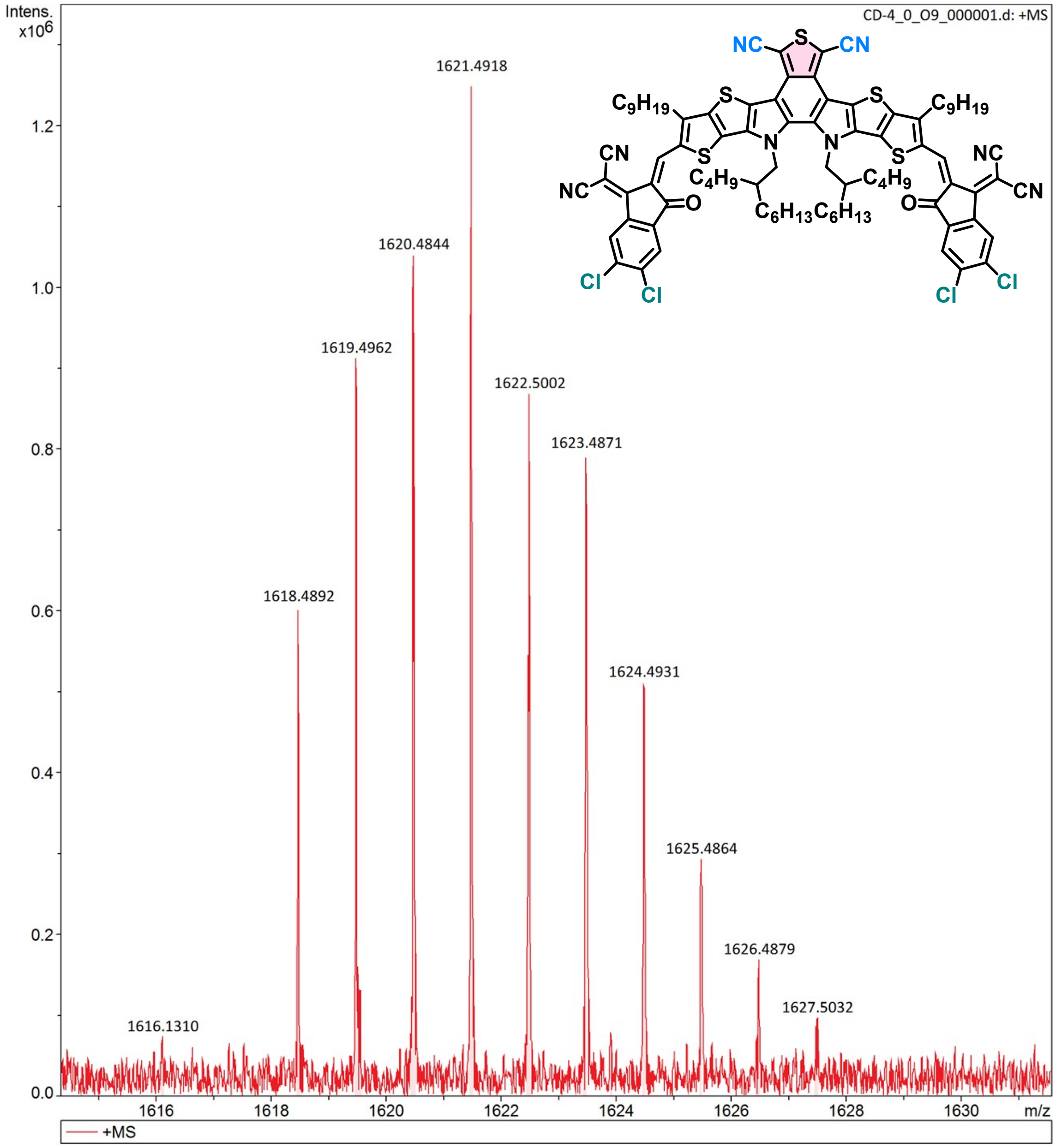

Figure S30. HR-MS spectrum of **CD-2**.

17. References

[1] T. Duan, W. Feng, Y. Li, Z. Li, Z. Zhang, H. Liang, H. Chen, C. Zhong, S. Jeong, C. Yang, S. Chen, S. Lu, O. A. Rakitin, C. Li, X. Wan, B. Kan, Y. Chen, *Angew. Chem. Int. Ed.* **2023**, *62,* e202308832.

[2] N. Beye, M. P. Cava, *J. Org. Chem.* **1994***, 59,* 2223–2226.

[3] S. Grimme, S. Ehrlich, L. Goerigk, *J. Comput. Chem.* **2011**, *32*, 1456-1465.

[4] T. M. Henderson, A. F. Izmaylov, G. Scalmani, G. E. Scuseria, *J. Chem. Phys.* **2009***, 131,* 044108.

[5] T. Lu, F. W. Chen, *J. Comput. Chem.* **2012**, *33*, 580-592.

[6] M. J. Frisch, G. W. Trucks, H. B. Schlegel, G. E. Scuseria, M. A. Robb, J. R. Cheeseman, G. Scalmani, V. Barone, G. A. Petersson, H. Nakatsuji, X. Li, M. Caricato, A. V. Marenich, J. Bloino, B. G. Janesko, R. Gomperts, B. Mennucci, H. P. Hratchian, J. V. Ortiz, A. F. Izmaylov, J. L. Sonnenberg, D. Williams-Young, F. Ding, F. Lipparini, F. Egidi, J. Goings, B. Peng, A. Petrone, T. Henderson, D. Ranasinghe, V. G. Zakrzewski, J. Gao, N. Rega, G. Zheng, W. Liang, M. Hada, M. Ehara, K. Toyota, R. Fukuda, J. Hasegawa, M. Ishida, T. Nakajima, Y. Honda, O. Kitao, H. Nakai, T. Vreven, K. Throssell, J. A. Montgomery, Jr., J. E. Peralta, F. Ogliaro, M. J. Bearpark, J. J. Heyd, E. N. Brothers, K. N. Kudin, V. N. Staroverov, T. A. Keith, R. Kobayashi, J. Normand, K. Raghavachari, A. P. Rendell, J. C. Burant, S. S. Iyengar, J. Tomasi, M. Cossi, J. M. Millam, M. Klene, C. Adamo, R. Cammi, J. W. Ochterski, R. L. Martin, K. Morokuma, O. Farkas, J. B. Foresman, D. J. Fox, Gaussian 16, **2016**, Revision C.01.

[7] https://gitee.com/coordmagic/xwtune

[8] J. Pommerehne, H. Vestweber, W. Guss, R. F. Mahrt, H. Bassler, M. Porsch, J. Daub, *Adv. Mater.* **1995**, *7*, 551-554.

[9] L. Krause, R. Herbst-Irmer, G. M. Sheldrick, D. Stalke, *J. Appl. Crystallogr.* **2015**, *48*, 3-10.

[10] G. M. Sheldrick, *Acta Cryst.* **2015**, *A71*, 3-8.

[11] G. M. Sheldrick, *Acta Cryst.* **2015**, *C71*, 3-8.

[12] O. V. Dolomanov, L. J. Bourhis, R. J. Gildea, J. A. K. Howard, H. Puschmann, *J. Appl. Cryst.* **2009**, *42*, 339-341.